International Journal of Nanomedicine

Dovepress

open access to scientific and medical research

Open Access Full Text Article

ORIGINAL RESEARCH

Precision USPIO-PEG-SLe^x Nanotheranostic Agent Targeted Photothermal Therapy for Enhanced Anti-PD-L1 Immunotherapy to Treat Immunotherapy Resistance

Ting Li[1,*], Lianshan Guo[2,*], Jiaxu Li[3,*], Xingyu Mu[4], Lijuan Liu[1], Shulin Song[1], Ningbin Luo[1], Qi Zhang[5], Bin Zheng[1], Guanqiao Jin[1]

[1]Department of Radiology, Guangxi Medical University Cancer Hospital, Nanning, 530021, People's Republic of China; [2]Department of Emergency, The Second Affiliated Hospital of Guangxi Medical University, Nanning, 530007, People's Republic of China; [3]Guangxi Key Laboratory of Natural Polymer Chemistry and Physics, College of Chemistry and Materials, Graduate School, Nanning Normal University, Nanning, 530001, People's Republic of China; [4]Department of Nuclear Medicine, Affiliated Hospital of Guilin Medical University, Guilin, 541001, People's Republic of China; [5]Laboratory Animal Center, Guangxi Medical University, Nanning, 530021, People's Republic of China

*These authors contributed equally to this work

Correspondence: Guanqiao Jin, Email jinguanqiao77@gxmu.edu.cn

Background: The anti-Programmed Death-Ligand 1 (termed aPD-L1) immune checkpoint blockade therapy has emerged as a promising treatment approach for various advanced solid tumors. However, the effect of aPD-L1 inhibitors limited by the tumor microenvironment makes most patients exhibit immunotherapy resistance.

Methods: We conjugated the Sialyl Lewis X with a polyethylene glycol-coated ultrasmall superparamagnetic iron oxide (USPIO-PEG) to form UPS nanoparticles (USPIO-PEG-SLe^x, termed UPS). The physicochemical properties of UPS were tested and characterized. Transmission electron microscopy and ICP-OES were used to observe the cellular uptake and targeting ability of UPS. Flow cytometry, mitochondrial membrane potential staining, live-dead staining and scratch assay were used to verify the in vitro photothermal effect of UPS, and the stimulation of UPS on immune-related pathways at the gene level was analyzed by sequencing. Biological safety analysis and pharmacokinetic analysis of UPS were performed. Finally, the amplification effect of UPS-mediated photothermal therapy on aPD-L1-mediated immunotherapy and the corresponding mechanism were studied.

Results: In vitro experiments showed that UPS had strong photothermal therapy ability and was able to stimulate 5 immune-related pathways. In vivo, when the PTT assisted aPD-L1 treatment, it exhibited a significant increase in $CD4^+$ T cell infiltration by 14.46-fold and $CD8^+$ T cell infiltration by 14.79-fold, along with elevated secretion of tumor necrosis factor-alpha and interferon-gamma, comparing with alone aPD-L1. This PTT assisted aPD-L1 therapy achieved a significant inhibition of both primary tumors and distant tumors compared to the alone aPD-L1, demonstrating a significant difference.

Conclusion: The nanotheranostic agent UPS has been introduced into immunotherapy, which has effectively broadened its application in biomedicine. This photothermal therapeutic approach of the UPS nanotheranostic agent enhancing the efficacy of aPD-L1 immune checkpoint blockade therapy, can be instructive to address the challenges associated with immunotherapy resistance, thereby offering potential for clinical translation.

Keywords: immunotherapy resistance, immune checkpoint blockade, nanotheranostic agent, photothermal therapy, enhancing efficacy

Introduction

According to data estimated by GLOBOCAN in 2020, cancer remains one of the leading causes of death globally.[1] Primary approaches for managing cancer encompass a range of strategies, such as surgical interventions to remove tumors, the administration of chemotherapy to attack cancer cells, utilizing radiation therapy to target and eliminate

Received: 7 November 2023
Accepted: 19 January 2024
Published: 7 February 2024

cancerous tissues, employing targeted therapy to specifically target cancer cells, utilizing hormone therapy to control hormone-driven cancers, and employing photodynamic therapy to produce reactive oxygen species (ROS) for killing cancer cells, etc.[2–5] However, due to the complexity of tumors and potential adverse effects such as resistance in radiation therapy and systemic toxicity induced by chemotherapy, traditional treatment strategies have some limitations in achieving the desired therapeutic outcomes. Recently, immune checkpoint blockade (ICB) has emerged as a promising approach in immunotherapy for a range of advanced solid tumors, including cases insensitive to platinum-based drug chemotherapy and those experiencing recurrence or metastasis.[6] Programmed Death-Ligand 1 (PD-L1) is present on the surface of tumor cells and is an immune inhibitory molecule that suppresses T-cell activation when binding to the programmed cell death 1 receptor (PD-1) on T lymphocytes. Monoclonal antibodies (mAb) targeting PD-L1 have the ability to block the interaction between PD-L1 and its receptor PD-1, which helps alleviate the inhibition of T lymphocytes and ultimately restores the immune response against malignant cells.[7] The US Food and Drug Administration (FDA) has approved PD-L1-targeting monoclonal antibodies for the treatment of various cancer types,[8,9] and ongoing clinical trials continue to explore the therapeutic potential of PD-L1-targeting antibodies.[10] However, over 60% of individuals with anti-PD-1/PD-L1 immunotherapy experiences resistance, and some face disease progression when receiving anti-PD-1/PD-L1 monotherapy.[11–13] The immunotherapy resistance may be caused by these factors: some tumor cells with relatively few gene mutations are not easily recognized by immune cells, and some tumor microenvironments are not suitable for immune cells to infiltrate or survive.[14] Therefore, the original immune cells in such tumors are too few, and the activation effect of PD-1/L1 inhibitors is limited. Furthermore, the more PD-L1 expressed by the tumor itself, the better the anti-tumor effect of PD-1/L1 inhibitors. Due to the significant limitations of current anti-PD-1/PD-L1 therapies, which hinder the achievement of desired outcomes, there is an urgent to explore methods that can effectively enhance the efficacy of anti-PD-1/PD-L1 treatments.[15–18]

As we strive to find suitable treatment strategies in conjunction with PD-1/PD-L1 antibodies, our focus has shifted towards an emerging paradigm of targeted therapy using nanomaterials and nanotechnology, the concepts that have garnered significant attention in recent years.[19–21] Among these, photothermal therapy (PTT) has gained widespread acclaim as a non-invasive and highly precise cancer management method. PTT utilizes nanomaterials capable of converting light energy into heat, inducing localized hyperthermia and selectively destroying cancer cells. PTT not only enables the local eradication of primary tumors, but also triggers immunogenic cell death (ICD). Therefore, PTT could elicit an immune response and reshape the tumor microenvironment.[22] During PTT, dying tumor cells release tumor-associated antigens, such as calreticulin (CRT) and high mobility group box 1 (HMGB1), as “eat me” signals, which are taken up by immature dendritic cells to induce dendritic cell maturation and T-cell activation, ultimately leading to an anti-tumor effect. Some preclinical studies have reported promising results about PTT combined with aPD-L1 treatment for cancer.[23–25] For instance, Tang et al investigated the use of supramolecular cationic gold nanorods-mediated PTT in combination with aPD-L1 antibodies for treating mouse tumor models, which has shown significantly suppressed primary and metastatic tumor activity compared to monotherapy with an enhanced anti-tumor immune response.[26] In a similar vein, Fang et al explored the combined utilization of synthetic MPX3-based PTT in conjunction with treatment targeting PD-L1 inhibition have demonstrated extension survival among experimental murine subjects.[27] However, these above reported nanomaterial’s synthesis methods are complex process and not conducive to clinical translation. Additionally, the biocompatibility of the nanomaterial is also a significant concern to be considered. Polyethylene glycol (PEG) is widely used to modify biomaterials due to its excellent water solubility.[28,29] As a non-ionic water soluble polymer, PEG can efficiently improve the biocompatibility of the material.

We have synthesized a versatile nanotheranostic agent named polyethylene glycol-coated ultrasmall superparamagnetic iron oxide nanoparticles coupled with sialyl Lewis X (USPIO-PEG-SLe^x, termed UPS) with excellent biocompatibility and strong dual-modal imaging capabilities (magnetic resonance imaging and thermal imaging) through a straightforward amidation synthesis method, comprising ultrasmall superparamagnetic iron oxide, polyethylene glycol, and sialyl Lewis X targeting moiety. Our group previous research demonstrated that it could achieve precise tumor targeting through targeting the SLe^x ligand to E-selectin-expressing tumor cells and tumor neoangiogenic endothelial cells.[30] E-selectin is a kind of transmembrane protein, which often expresses in the vascular

endothelial cells of inflammation or cancer.[30,31] And E-selectin relates to the progression, metastasis and prognosis of a variety of malignant tumors, such as breast cancer, gastric cancer, and nasopharyngeal carcinoma. The specific ligand of E-selectin is namely sialyl Lewis X. Based on our and others studies, we hypothesized that our UPS nanoparticles prepared could not only exert photothermal ablation effect, but also have the potential to stimulate the immune system response. The underlying mechanism of our UPS nanoparticles is that PTT stimulates the immune system in vivo, remodels the immune microenvironment, improves the effect to resist the immunotherapy resistance, and enhances the systemic immune response to tumors. In order to treat the immunotherapy resistance, for the first time, we investigate the ability of UPS-mediated PTT to stimulate the proliferation of $CD4^+$ T cells and $CD8^+$ T cells, enhancing the efficacy of aPD-L1 immunotherapy through precise tumor targeting, local hyperthermia, and immune system regulation. The therapy function was performed in a mouse model of head and neck squamous cell carcinoma (HNSCC), as shown in Figure 1.

Materials and Methods

Reagents

3'-sialyl Lewis X (termed SLe^x) (Carbosynth, UK), Fe_3O_4@OA@DSPE-PEG2k-NH_2 (Nanjing Nanoeast Biotech Co., Ltd.), 2- (N-morpholino) ethanesulfonic acid (MES) (TMLT40545500MG, China National Pharmaceutical Group Corporation Chemical Reagent Company), 1-(3-dimethylaminopropyl)-3-ethylcarbodiimide (EDC) (Sigma), 808 nm near-infrared laser (BWT, Beijing, China), anti-mouse PD-L1 (B7-H1) in vivo monoclonal antibody (Selleck), high mobility group box 1 (HMGB1) antibody (AF7020, Affinity Biosciences Ltd.), calreticulin (CRT) antibody (DF6211, Affinity Biosciences Ltd.), recombinant anti-CD4 antibody (ab183685, Abcam), recombinant anti-CD8 alpha antibody (ab217344, Abcam).

Synthesis of the Nanotheranostic Agent UPS

The synthesis method of the nanotheranostic agent UPS refers to the previous literatures.[32,33] Initially, a solution of 5 mg SLe^x was prepared in 1 mL of sterile distilled water, resulting in a concentration of 5 mg mL^{-1}. Subsequently, 200 μL of this solution was divided into 5 tubes, each containing 1 mg. Two of these tubes were further diluted by adding 800 μL of pure water, achieving a concentration of 1 mg mL^{-1}. Next, a conical flask equipped with a mechanical stirrer set at 500 rpm was charged with 11 mL of Fe_3O_4@OA@DSPE-PEG2k-NH_2 solution (1 mg mL^{-1}). The pH was adjusted by adding 2.2 mL of 0.015 mol L^{-1} MES buffer (pH 5.5). In the subsequent step, 1.2 mL of SLe^x solution (1 mg mL^{-1}) was mixed with 200 μL of 0.015 mol L^{-1} MES buffer (pH 5.5) to attain the desired pH. This mixture was then added to the previous step while vortexing, followed by incubation in a 37 °C water bath for 30 minutes. For the fourth step, 300 μL of EDC (10 mg mL^{-1}, dissolved in 0.015 mol L^{-1} MES buffer, pH 5.5) was introduced, equivalent to 3 mg, and the solution was vortexed and incubated overnight at 37 °C. Finally, the solution underwent four rounds of ultrafiltration using a 100 KD ultrafiltration tube with pure water to eliminate excess EDC and unreacted SLe^x. The post-ultrafiltration suspension was diluted with pure water to achieve a final volume of 10 mL, and the iron concentration was quantified using the o-phenanthroline absorption spectrophotometric method. The obtained UPS nanoparticles aqueous solution was ultimately adjusted to a final iron concentration of 1 mg mL^{-1}. The procurement and synthesis of reagents were outsourced to Nanjing Nanoeast Biotech Co., Ltd., and the detailed synthetic steps were provided by the same company.

Physicochemical Characterization of UPS Nanoparticles

The size and morphology of UPS were assessed using a high-resolution transmission electron microscope (HT7800, Hitachi). The hydrodynamic size and zeta potential of USPIO-PEG and UPS were analyzed using a specialized nanoparticle size and zeta potential analyzer (Zetasizer Lab, Malvern Panalytical Ltd., UK). The magnetic properties of UPS were precisely determined using a Vibrating Sample Magnetometer (VSM) (Model 7404, LakeShore Corporation, USA).

The near-infrared absorption spectra of UPS at different concentrations (25 μg mL^{-1}, 50 μg mL^{-1}, 100 μg mL^{-1}, and 200 μg mL^{-1}) were measured using the ultraviolet spectrophotometry. The near-infrared absorption spectra of UPS were measured using the ultraviolet spectrophotometry both without laser irradiation and after 10 minutes of irradiation with

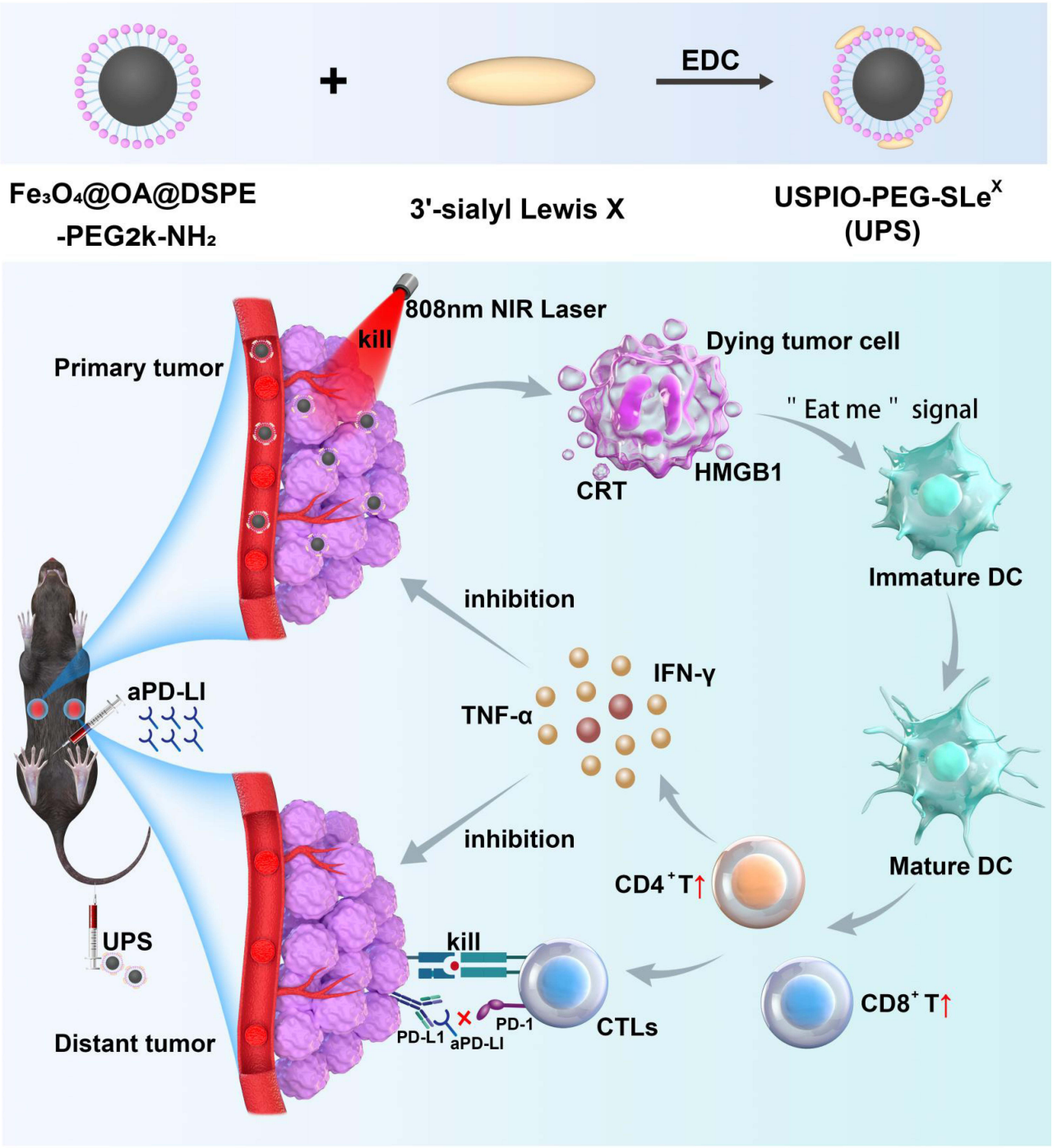

Figure 1 Schematic representation illustrating the specific accumulation of amidation-synthesized UPS nanoparticles within tumor sites, facilitating PTT and enhancing aPD-L1 immunotherapy to eliminate the tumors. When the 808 nm laser irradiates the primary tumors, the UPS nanoparticles produce photothermal effect to kill the primary tumor cells. And the dying tumor cell induces ICD, releasing CRT and HMGB1, stimulating the proliferation of $CD4^+$ T cells and $CD8^+$ T cells, along with increased secretion of TNF-α and IFN-γ. Meanwhile, the aPD-L1 blocks PD-L1 on tumor cells. Finally, the activating cytotoxic T lymphocytes (CTLs) kill distant tumors, and the TNF-α and IFN-γ inhibit the recurrence of primary tumors and distant tumors.

the 808nm near-infrared laser (2.1 W cm^{-2}). The characterization works, including high-resolution transmission electron microscopy, hydrodynamic size, zeta potential, and VSM measurements, were meticulously conducted by Nanjing Nanoeast Biotech Co., Ltd., ensuring the accuracy and reliability of the results.

UPS Nanoparticles in vitro Photothermal Characteristics

A 1 mL solution of UPS with a concentration of 100 μg mL^{-1} was placed in a cuvette. Subsequently, the solution was exposed to 808 nm laser irradiation (2.1 W cm^{-2}) in a continuous heating-cooling cycle repeated five times to assess the photothermal conversion stability of UPS. A 1 mL solution of UPS at a concentration of 100 μg mL^{-1} was irradiated with the 808 nm laser (2.1 W cm^{-2}) for 10 minutes, and temperature changes during the heating-cooling process were recorded. Subsequently, the photothermal conversion efficiency (η) of UPS was calculated using the method previously reported.[34] The η is calculated using the following formula:

$$\eta = (h \times S \times (T_{max} - T_s) - Q_s) / (I \times (1 - 10^{(-A_\lambda)}))$$

Here, h and S denote the coefficient of heat transfer and the surface area of the sample vessel, respectively. T_{max} and T_s indicate the maximum temperature reached by the dispersed sample in its steady state and the surrounding environment's temperature, correspondingly. Q_s represents the baseline energy input derived from the solvent and sample vessel in the absence of nanoparticles, which was independently determined using pure deionized water. I signifies the laser's power, while A_λ refers to the nanoparticles' absorbance at the wavelength of 808 nm. A 1 mL solution with a concentration of 200 μg mL^{-1} of UPS was irradiated with the 808 nm laser at the intensity of 2.1 W cm^{-2} for 5 minutes, during which infrared thermal images were captured using an infrared thermal imaging device.

Cell Culturing and Treatment

Human nasopharyngeal carcinoma cells (5–8F cell) and squamous cell carcinoma 7 (SCC7) were nurtured in a complete growth medium comprising 10% fetal bovine serum, 1% solution of penicillin and streptomycin, along with 90% RPMI-1640 medium (manufactured by Gibco) (v/v). The cellular cultures were upheld in a precisely controlled environment, specifically within a cell culture incubator established at a temperature of 37 °C with a CO_2 concentration of 5%. Cell experiments were all irradiated using the 808 nm near-infrared (NIR) laser.

Cellular Uptake Analysis Using Transmission Electron Microscopy

The UPS nanoparticles (200 μg mL^{-1}) were co-cultured with 5–8F cells (5×10^5 cells/well) for 4 hours, pre-fixed with 3% glutaraldehyde, post-fixed with 1% osmium tetroxide, gradually dehydrated with acetone, embedded in Epon812, semi-thin sections were stained with toluidine blue for optical localization, ultra-thin sections were prepared using a diamond knife, and then stained with uranyl acetate and lead citrate for observation under a JEM-1400FLASH Transmission Electron Microscope.

Cellular Uptake Determination Using ICP-OES

To determine the cellular uptake, 5–8F cells were seeded in 6-well plates with a density of 5×10^5 cells per well overnight. Subsequently, cells were incubated with UPS nanoparticles or USPIO-PEG nanoparticles at an iron concentration of 200 μg mL^{-1}. After incubation at 37 °C for 1 h, 6 h and 12 h respectively, the cells were then washed with PBS for three times and lysed by cell lysis buffer. The iron content in the cell lysis solution was determined by ICP-OES (ThermoICPOES7200, USA).

Flow Cytometry for Detecting Cell Apoptosis

5–8F cells (5×10^5 cells/well) were co-incubated with UPS (100 or 200 μg mL^{-1}) for 4 hours in different groups (37 °C, 5% CO_2). The laser irradiation group received the 808 nm near-infrared laser with the intensity of 2.1 W/cm^2 to irradiate the cancer cells for 10 min. After continued incubation for 24 hours, detection was performed using the Annexin V-FITC cell apoptosis detection kit and a flow cytometer.

Mitochondrial Membrane Potential Detection in Early Apoptosis

5–8F cells (5×10^5 cells/well) were inoculated into a 6-well plate with 2 mL complete medium per well and cultured for 12 hours. The control group was not treated, and the 5–8F cells of the experimental group were

incubated with UPS (200 μg mL^{-1}) for 4 h, treated with 808 nm laser (2.1 W cm^{-2}) for 10 min, and then incubated in a cell incubator containing 5% CO_2 at 37 °C for 4 hours. The medium was removed and stained according to the Mitochondrial Membrane Potential Assay Kit with JC-1 (Solarbio). The cells were washed and the images were collected under a fluorescence microscope.

Live and Dead Cell Staining for Cell Apoptosis Study

5–8F cells were seeded in 6-well plates at a density of 5×10^5 cells/well and cultured for 12 h. Cells were then incubated with UPS nanoparticles at a final Fe concentration of 100 μg mL^{-1} or 200 μg mL^{-1} for 4 h. The laser irradiation group received the 808 nm near-infrared laser with the intensity of 2.1 W/cm^2 to irradiate the cancer cells for 10 min. After being incubated for 24 h, the cells were stained by Live/Dead Viability/Cytotoxicity Assay Kit, according to the manufacturer's protocol, and then observed by fluorescence microscope.

Suppression of in vitro Cell Migration

A scratch insert was positioned at the base of a 6-well culture plate, and 5–8F cells (4.2×10^4 cells/well) were uniformly dispensed within the insert. Following the formation of an adherent cell monolayer, the insert was gently withdrawn, and PBS was employed to eliminate unattached cells prior to the introduction of fresh medium supplemented with 5% FBS. Varied experimental groups were established, wherein UPS (100 or 200 μg mL^{-1}) were included according to the grouping scheme. For the laser irradiation cohort, exposure to 808 nm near-infrared laser with the intensity of 2.1 W/cm^2 to irradiate the cancer cells for 10 min was implemented. Visual documentation was performed at the 0-hour, 6-hour, and 12-hour marks.

RNA-Sequencing Analysis of Tumor Cells

5–8F cells (1×10^6 cells/well) were seeded in a 6-well plate with 2 mL of complete medium per well and cultured for 12 hours. They were divided into two groups: the control group and the PTT group, each with three replicates. The control group was treated with PBS, while the PTT group was treated with 200 μg mL^{-1} of UPS. After 4 hours, the cells were exposed to the 808 nm laser (2.1 W cm^{-2}) for 10 minutes. Following 24 hours of culture, RNA from the cells was extracted using TRIzol reagent. The samples were sent to Sangon Biotech (Shanghai) Co., Ltd. for RNA-sequencing. The sequencing results were analyzed to generate co-expression Venn diagrams, volcano plots, heat maps, kyoto encyclopedia of genes and genomes (KEGG) pathway maps, and protein-protein interaction networks.

In vitro Hemolysis Assay

Utilizing the ocular blood collection technique, whole blood samples were obtained from mice of sound health and subsequently introduced into tubes preloaded with EDTA, an anticoagulant agent. After thorough shaking, the tubes underwent centrifugation at 3000 r/min for the duration of 15 min, facilitating the separation of blood cells. Different levels of UPS solution (25 μg mL^{-1}, 50 μg mL^{-1}, 100 μg mL^{-1}, and 200 μg mL^{-1}), along with PBS (negative control value, -) and pure water (positive control value, +) (1 mL each), were combined with 20 μL of blood cells based on the assigned groupings. After a 4-hour period of incubation within a cell culture chamber, the specimens underwent centrifugation at a speed of 3000 r/min for the duration of 15 min, followed by subsequent image acquisition. The supernatant was gathered for spectrophotometric assessment at a wavelength of 540 nm utilizing an ELISA measurement device. Every experiment was executed three times, and the mean value was computed. The calculation of hemolysis percentage was performed using the subsequent formula: $\text{Hemolysis rate}(\%) = (\text{Sample value} - \text{Negative control value}) / (\text{Positive control value} - \text{Negative control value}) \times 100\%$.

Animal and Tumor Models

Male C57BL/6J mice without specific pathogens were obtained from SPF (Beijing) Biotechnology Co., Ltd. The mice were accommodated within the facilities of Guangxi Medical University's Experimental Animal Center. Ethical evaluation of animal experiments adhered to the guidelines established by the Ministry of Science and Technology of the People's Republic of China, as well as the National Standard GB/T35892-2018, titled Ethical Standards for Animal Welfare in Experimental Research. Tumor dimensions were computed using the formula: length × $width^2$ × 0.5. The

animal experiments utilized the SCC7 tumor model. Each male C57BL/6J mouse received a subcutaneous injection of cell suspension (50 μL, 5×10^5 cells) to establish primary tumors in the right axilla and simultaneously injected the same cell suspension in the left axilla to establish distant tumors. The mice carrying the SCC7 model were randomly assigned to groups (n = 5 per group): Control group (Group 1); aPD-L1 treatment group (Group 2); PTT alone group (Group 3); PTT-assisted aPD-L1 treatment group (Group 4). When tumors reached approximately 100 mm^3, treatment was commenced, with the tumor growth volume and mouse weight changes were recorded.

In vivo Biosafety Assessment

The experiment included a PBS group (n = 3) and an experimental group (n = 3). 15.5 mg kg^{-1} solution was intravenously injected into C57BL/6J mice, with a dose administered every two days for a total of five doses. Mouse weights were recorded, and on the 10th day, blood was drawn from the orbital cavity for blood routine analysis. The residual blood was gathered into 1.5 mL EP tubes, left at ambient temperature for 2 hours, followed by centrifugation at 4 °C, 3000 rpm for 15 min. The supernatant was preserved at −80 °C for subsequent analysis of blood biochemistry. Mice were dissected, and organs including the heart, liver, spleen, lung, and kidney underwent fixation using 4% paraformaldehyde over the duration of 24 hours. Histopathological examination was conducted through H&E staining.

In vivo Pharmacokinetics

Mice (n = 3) were intravenously injected with 800 μL of UPS solution at a iron concentration of 1 mg mL^{-1}. Blood samples were collected from the orbital cavity at specified time intervals: 5 min, 10 min, 20 min, half an hour, 1 h, 2 h, 4 h, 8 h, 12 h, and 24 h, for the purpose of blood pharmacokinetic analysis utilizing ICP-OES.

In vivo Photothermal Impact of UPS Nanoparticles

As outlined earlier, a tumor model was established, and the mice were categorized into both an untreated cohort and a photothermal therapy (PTT) cohort. A tail intravenous administration of UPS aqueous solution (15.5mg kg^{-1}) was performed. After the UPS aqueous solution injection of 1 h, an irradiation of the tumor site with the 808 nm laser (2.1 W cm^{-2}) for the duration of 5 min. This procedure was carried out while concurrently capturing thermal images using an infrared thermal imaging camera.

UPS Nanoparticle Mediated PTT Enhances the Therapeutic Efficacy of aPD-L1 in Treating Primary Tumors and Distant Tumors

The effect of UPS-mediated PTT on immunogenic cell death and its enhancement of the aPD-L1 immune checkpoint inhibitor's impact on both primary and distant tumors using the SCC7 tumor model were investigated. Each male C57BL/6J mouse received a subcutaneous injection of cell suspension (50 μL, 5×10^5 cells), establishing primary tumors in the right axilla and distant tumors in the left axilla with an equivalent cell suspension injection. The SCC7-bearing mouse models were randomly assigned to groups in a randomized manner (each with n = 5): Control (Group 1); aPD-L1 treatment (Group 2); PTT alone (Group 3); and PTT assists aPD-L1 treatment (Group 4). Mice in Groups 3 and 4 received intravenous injections of UPS solution (15.5mg kg^{-1}) on days 0, 2, and 4. After an hour, primary tumors in these groups were subjected to 808 nm laser irradiation (2.1 W cm^{-2}) for 10 minutes. Meanwhile, mice in Groups 2 and 4 received intraperitoneal injections of aPD-L1 (1 μg kg^{-1}) on days 0, 2, and 4. We recorded the daily body weight and tumor diameter of the mice. On day 6, mice were anesthetized, and blood samples were collected to separate serum. Enzyme-linked immunosorbent assay (ELISA) was used to quantify the levels of TNF-α and IFN-γ. The primary and distant tumors of each group of mice were dissected and photographed. Primary tumors were analyzed using H&E staining, Ki67 staining, and immunofluorescence staining for CRT and HMGB1. Distant tumor sections underwent $CD4^+$ and $CD8^+$ T cell immunofluorescence staining, TUNEL immunofluorescence staining, and evaluation of tumor proliferation using PCNA staining. Additionally, major organs from each group of mice were dissected and subjected to H&E staining for histological evaluation.

Statistical Methodology

The data is presented as mean ± standard deviation or SEM. To assess differences among multiple groups, we employed one-way analysis of variance (ANOVA). A significance level of $\alpha = 0.05$ was chosen, whereby P-values of less than 0.05 were deemed statistically noteworthy and indicated with *while P-values less than 0.01 were marked as **those less than 0.001 were annotated as ***and P-values less than 0.0001 were represented by ****.

Results and Discussions

Physicochemical characterization and in vitro photothermal properties of UPS nanoparticles

The physicochemical properties of nanoparticle play a pivotal role in determining their application potential. In this comprehensive analysis, we delved into various aspects of UPS nanoparticles, shedding light on their distinct characteristics and how these attributes to their suitability for photothermal therapy. The TEM images divulged the morphology and dimensions of the synthesized UPS nanoparticles, reaffirming their consistent alignment with previous nanoparticle iterations developed by our research team.[30] These nanoparticles maintained an average diameter of approximately 10 nm, encompassing both square and circular shapes (Figure 2A). The observed uniformity underscores the reproducibility of our synthesis methodology and the predictive nature of their size and shape, both critical facets for achieving consistent and desired therapeutic outcomes. The hydrodynamic diameters of the USPIO-PEG and UPS solutions were meticulously assessed and recorded as 20.91 ± 0.50 nm and 42.38 ± 1.07 nm, respectively (Figure 2B and C). This increase in size subsequent to coupling signifies the effective incorporation of

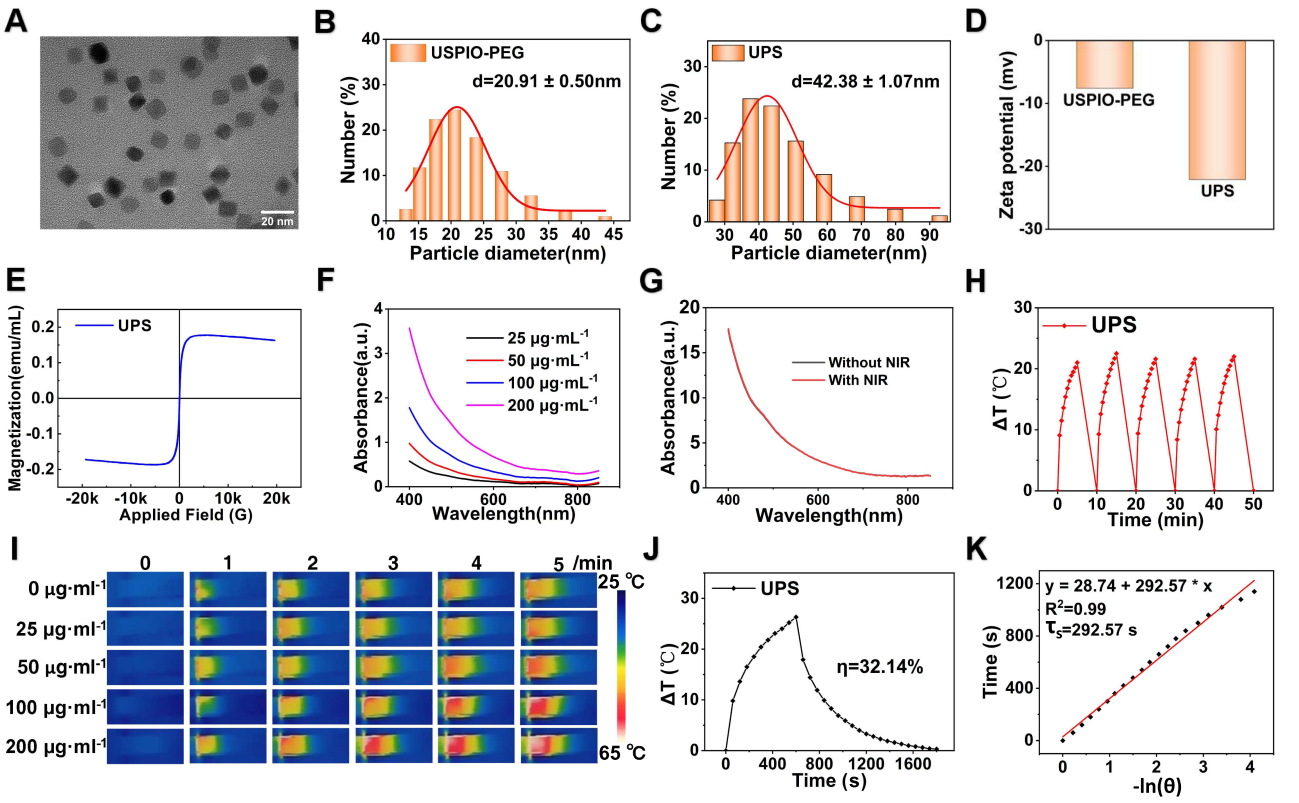

Figure 2 Physicochemical characterization and photothermal performance of UPS nanoparticles. (**A**) Schematic representation of the nanostructure of UPS as observed by transmission electron microscopy (TEM). (**B**) Particle dimensions for the USPIO-PEG formulation. (**C**) Nanoparticle size of the UPS complex. (**D**) Zeta potentials assessed for USPIO-PEG and UPS. (**E**) Evaluation of magnetic properties through Vibration Sample Magnetometer (VSM) analysis for the UPS nanoparticles aqueous solution. (**F**) Optical UV-vis-near-infrared (NIR) absorption spectra of UPS nanoparticles aqueous solution at different concentrations. (**G**) Optical UV-vis-NIR absorption spectra of UPS nanoparticles aqueous solution (1 mg mL^{-1}) with and without near-infrared light irradiation (808nm laser, 2.1 W cm^{-2}). (**H**) Study of photothermal stability of 1 mL UPS nanoparticles aqueous solution (100 μg mL^{-1}) during five cycles of heating-cooling processes (808nm laser, 2.1 W cm^{-2}). (**I**) In vitro thermal imaging of UPS. (**J**) Heating and cooling curves of 1 mL UPS nanoparticles aqueous solution (100 μg mL^{-1}) and photothermal conversion efficiency (808nm laser, 2.1 W cm^{-2}). (**K**) Negative logarithm plot of cooling time of UPS against temperature driving force.

sialyl Lewis X (SLe^x), potentially fostering enhanced interactions with cellular targets. And the zeta potential of USPIO-PEG and UPS is −7.58 mV to −22.11 mV, respectively (Figure 2D). The shift towards a more negative zeta potential after SLe^x modification also indicates that SLe^x effectively occupies the amino groups on the surface of the USPIO-PEG, confirming successful coupling. The zeta potential of UPS nanoparticles is more negative than that of USPIO-PEG, due to the grafting SLe^x on USPIO-PEG through amidation reaction. The molecule composition of USPIO-PEG was expressed as Fe_3O_4@OA@DSPE-PEG2k-NH_2. And the active group modified on its surface is -NH_2, which only accounts for 10~15% in the molecule formula. However, a group of the higher proportion in the molecule formula is -O-CH_2- of the PEG2k. Therefore, the overall potential of UPSIO-PEG nanoparticles is slightly negative. These can be demonstrated by the negative zeta potential of pure -O-CH_2- particles. And the only carboxyl groups in SLe^x exist in the form of amide bonds and belong to uncharged groups. Furthermore, the hydroxyl groups on the SLe^x molecule structure are uncharged, but there are some epoxy groups and C=O, which will show a slight electronegativity. Therefore, even if SLe^x is not considered to have a negative charge, it is only neutral. Thus, even when SLe^x is considered to be uncharged and SLe^x is coupled to the surface of UPSIO-PEG via amidation synthesis method, SLe^x formed an uncharged amide bond with the original -NH_2 of UPSIO-PEG. And parts of the positive charge of -NH_2 were shielded, thus the synthetically obtained UPS nanoparticles overall tends to have a more negative potential. The magnetic behavior of UPS nanoparticles aqueous solution at room temperature was investigated by VSM testing (Figure 2E). The saturation magnetization (M_s) value of the UPS nanoparticles aqueous solution is 0.18 emu mL^{-1}, VSM unequivocally confirming the superparamagnetic behavior of the UPS nanoparticles. This characteristic plays a vital role in categorizing them as proficient contrasting agents in various medical imaging techniques, encompassing modalities such as magnetic resonance imaging (MRI). The ability of magnetic moments to respond to external magnetic fields enhances signal intensity, facilitating precise disease localization and status assessment. This capability is particularly significant during therapeutic interventions. It enables real-time monitoring of nanoparticle effects and allows for dynamic adjustments to treatment strategies. And the MRI functionality of UPS nanoparticles has been previously validated in our earlier study.[30] The UV-vis-NIR absorption spectra analysis of UPS solutions at varying concentrations (25–200 μg mL^{-1}) unveiled broad absorption bands within the NIR region (Figure 2F). The absorption pattern displayed a proportional enhancement with the elevation of UPS nanoparticle levels. The absorbance spectra of UPS nanoparticles aqueous solution before and after exposure to 808nm NIR laser showed negligible changes, demonstrating robustness of UPS under laser irradiation effects (Figure 2G).

The assessment of functionalized nanoparticles hinges upon critical parameters, namely, photothermal stability and photothermal conversion efficiency. The enduring photostability was manifest in temperature fluctuations upon exposure to 808nm laser radiation, even after the UPS nanoparticles underwent five cycles (Figure 2H). This observation strongly supports the capacity of nanoparticles (NPs) to withstand the rigors of repeated photothermal applications. And the Infrared thermal imaging elegantly demonstrated the photothermal effects of UPS NPs at different concentrations, revealing a proportional increase in temperature with rising nanoparticle concentration (Figure 2I). When the UPS NPs aqueous solution with a concentration of 200 μg mL^{-1} in 1 mL plastic centrifuge tube was irradiated with 808 nm laser at 2.1 W cm^{-2}, revealing, the temperature could nearly rise to 65 °C. Research findings indicate that hyperthermia at temperatures exceeding 48 °C can induce cellular necrosis, while comparatively milder temperatures in the range of 41–45 °C can impede cellular activity and promote the upregulation of heat shock proteins.[35] Therefore, through controlling the UPS NPs aqueous solution concentration and the laser irradiation conditions, the photothermal effect of UPS NPs can effectively killing cancer cells. The correlation between cooling duration and the negative natural logarithm of the temperature gradient was determined during the cooling phase (Figure 2K). The time constant (τ) of the UPS NPs was calculated to be 292.57s. Leveraging τ, the η value of UPS NPs at a concentration of 0.1 mg mL^{-1} was computed to be 32.14% (Figure 2J). These efficiency figures are closely to the competitive IID-ThTPA nanoparticles, whose τ and η is 442.68 s and 35.4%, respectively,[36] further affirming the promising photothermal capabilities of UPS NPs. To sum up, this collective evidence definitively establishes UPS NPs as potent contenders for photothermal therapy with magnetic resonance imaging and photothermal imaging, boasting remarkable photostability and material properties that align favorably with effective tumor nanotheranostic treatment.

In vitro Cellular Uptake and Therapeutic Effect of UPS Nanoparticle

The effectiveness and capabilities of nanoparticles in biomedical applications hinge on their interactions with targeted cells and subsequent responses. In our study, we delved into the cellular behavior and photothermal effects of UPS NPs in vitro, aiming to ascertain their potential for cancer therapy. The TEM images direct visualization underscores the internalization of UPS NPs by cancer cells, the critical prerequisites for successful therapeutic interventions (Figure 3A). These TEM images indicate their effective uptake to the intracellular of the tumor. To assess the in vitro cellular uptake of UPS nanoparticles, UPS nanoparticles with the targeting moiety Sle^x (200 μg mL^{-1}) were compared to USPIO-PEG nanoparticles (200 μg mL^{-1}) as a control. The cellular uptake of Fe content was measured using Inductively Coupled Plasma Optical Emission Spectroscopy (ICP-OES). As shown in Figure 3B, the intracellular Fe uptake increased over time. At 1 hour, 6 hours, and 12 hours, the cellular uptake in the UPS-treated group was significantly higher compared to the uptake in the USPIO-PEG group, indicating a statistically significant difference. This suggests that the modification with Sle^x effectively enhances the intracellular uptake of UPS nanoparticles. To assess the potential therapeutic efficacy of UPS nanoparticles in vitro, we employed a 5–8F cell model and investigated their photothermal effects. Insights into cell death rates were gleaned through the utilization of Annexin V-FITC/PI staining in the context of flow cytometric analysis (Figure 3C). Notably, minimal cell death was observed in the control and laser alone groups. Exposure to varying concentrations of UPS nanoparticles demonstrated low toxicity, with cell death rates of 4.32% and 5.12% at concentrations of 100 μg mL^{-1} and 200 μg mL^{-1}, respectively. Strikingly, the combination of UPS nanoparticles and NIR laser treatment induced substantial cell death, reaching 38.66% and 78.99%. With the augmentation of the UPS nanoparticles' aqueous solution concentration, there was a corresponding reduction in the viability of cancer cells following co-cultivation and irradiation treatment, indicating a dose-dependent photothermal cytotoxic effect. This outcome highlights the potent photothermal effect of the nanoparticles, a fundamental characteristic for effective PTT. To assess the tumor cells apoptosis after the PTT produced by UPS under 808 nm NIR irradiation, the changes of mitochondrial membrane potential were detected by mitochondrial membrane potential assay kit with JC-1 (JC-1) staining (Figure 3D). In normal mitochondria, JC-1 in the form of polymer showed red fluorescence, while in the damaged mitochondria, JC-1 in the form of monomer showed green fluorescence. After 0.2 mg mL^{-1} UPS nanoparticles combined with 2.1 W cm^{-2}808 nm NIR laser for 10min irradiation to treat the 5–8F cells, the green fluorescence was significantly enhanced, which was consistent with the green fluorescence shown in the positive group treated with Carbonyl cyanide m-chlorophenyl hydrazone (Cccp), while the control group showed strong red fluorescence. These results demonstrate UPS nanoparticle mediated PTT could lead to changes in mitochondrial membrane potential and dysfunction of mitochondrial function leading to cell apoptosis. And the calcium orange AM/PI double-staining experiments supported the trends observed in flow cytometry, confirming the significant cell death induced by UPS nanoparticles and NIR laser treatment (Figure 3E). Moreover, the migration tests revealed that laser alone treated cancer cells exhibited migration patterns similar to untreated cells, while UPS nanoparticle treatment suppressed migration (Figure 3F). It is worth noting that the PTT treatment group not only inhibited migration but also reduced cell density within 12 hours, which indirectly corroborated that the PTT treatment group could induce cell death. The quantitative analysis of migration experiments (Figure 3G) showed no statistical difference between the group treated solely with near-infrared light and the control group. This suggests that solely applying 808nm laser irradiation cannot inhibit cell migration. However, significant differences were observed between the group treated with UPS nanoparticles and the control group, indicating the effective inhibition of cell migration by UPS nanoparticles. Therefore, these various detection methods used have highlighted that the photothermal effect generated by UPS under 808nm laser can effectively kill cancer cells or inhibit cancer cells migration in vitro.

RNA-Sequencing Analysis of UPS Nanoparticle Mediated by PTT

To evaluate the cytotoxic mechanism of UPS nanoparticle mediated PTT and the potential mechanism of immune activation, genome-wide RNA-sequencing was performed on 5–8F cells under different treatment conditions. This assessment examined the transcription of 16728 genes. In these genes, 624 genes were transcribed in the PTT-treated cells (Figure 4A). In contrast to the PBS control cohort, the PTT group demonstrated upregulation in 87 genes (depicted

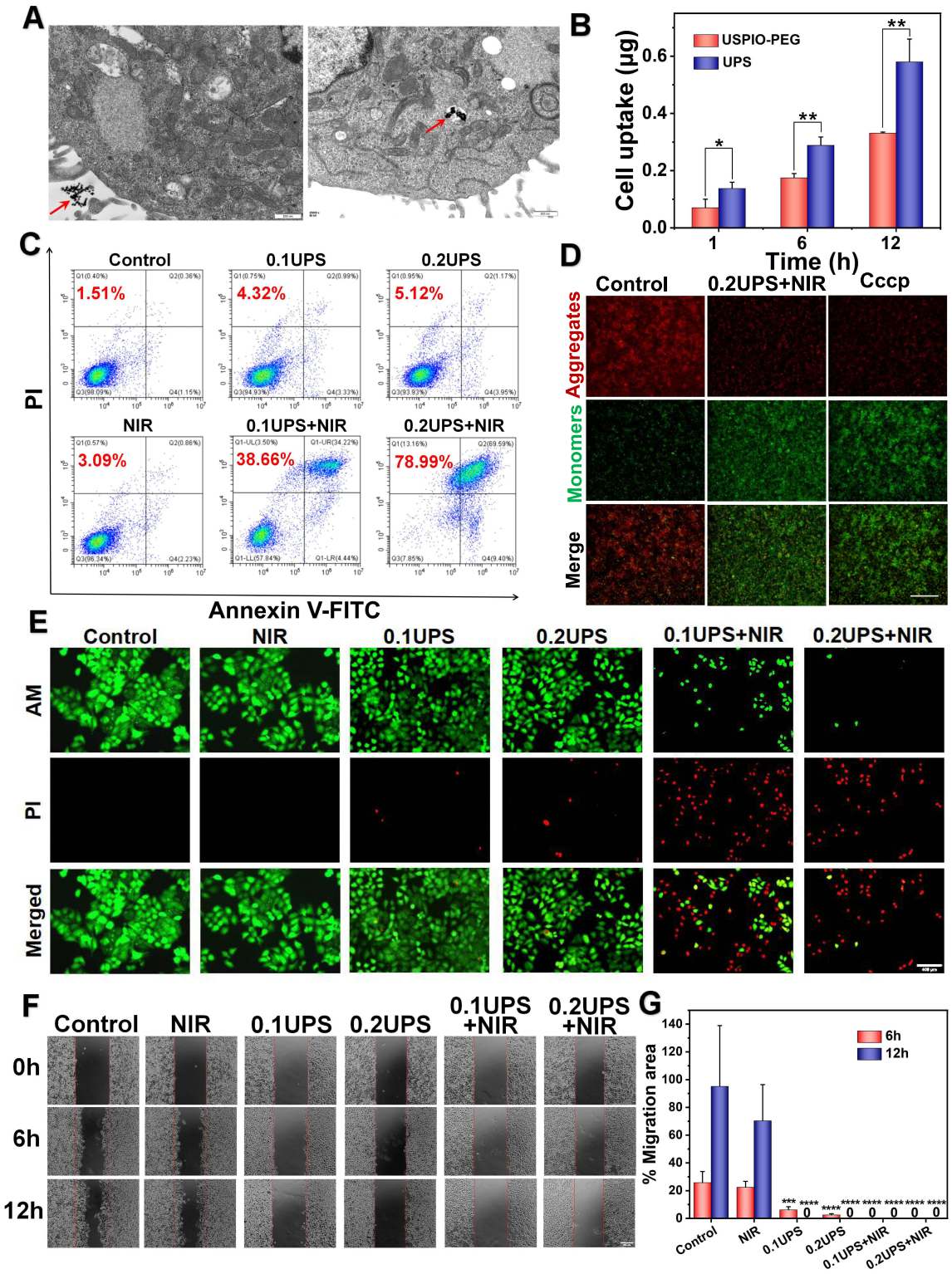

Figure 3 Tumor cellular uptake and anticancer effect in vitro. (**A**) TEM observation of cellular uptake of UPS nanoparticles by 5–8F cells (scale bar: 500 nm). On the left, the UPS nanoparticle initiates contact with the surface of the 5–8F cell. On the right, UPS nanoparticle is endocytosed by 5–8F cell. The red arrow indicates the UPS. (**B**) Quantitative analysis by ICP-OES of the uptake of USPIO-PEG (200 μg mL^{-1}) and UPS (200 μg mL^{-1}) by 5–8 cells at different time points. (**C**) Evaluation of apoptosis in 5–8F cells post diverse treatments using flow cytometry analysis. 0.1UPS: UPS nanoparticles aqueous solution with a concentration of 100 μg mL^{-1}; 0.2UPS: UPS nanoparticles aqueous solution with a concentration of 200 μg mL^{-1}; NIR: 808 nm laser irradiation. (**D**) The alteration in mitochondrial membrane potential of 5–8F cells following various treatments (scale bar: 200 μm). (**E**) Fluorescence microscopy images of live and dead cells staining after different therapeutic interventions in 5–8F cells (scale bar: 400 μm). (**F**) Migration status of 5–8F cells following distinct interventions (scale bar: 400 μm). (**G**) Quantitative analysis of cell migration in different treatment groups at 6 hours and 12 hours.
Notes: *Representing $p < 0.05$, **$p < 0.01$, and ***$p < 0.001$, and ****$p < 0.0001$, based on a sample size of n = 3.

as red dots), alongside downregulation in 230 genes (illustrated as green dots) (Figure 4B). Following PTT, we conducted Kyoto Encyclopedia of Genes and Genomes (KEGG) pathway enrichment analysis, which revealed the activation of five immune-related pathways: the RIG-I-like receptor signaling pathway, B cell receptor signaling pathway, protein processing in endoplasmic reticulum, Jak-STAT signaling pathway, and tumor necrosis factor (TNF) signaling pathway (Figure 4C). RIG-I-like receptor signaling pathway is an immune signaling pathway that is involved in recognizing viral infection and inducing immune response. B cell receptor signaling pathway is an immune receptor signaling pathway of B cells, which is involved in antibody production and immune response. The protein processing in endoplasmic reticulum is a signaling pathway about the immune cell activity and immune response, which included in participating in antigen processing and presentation, as well as regulating cytokine and immunoglobulin synthesis. It is essential for maintaining the normal function of the immune system and immune response. The Jak-STAT signaling pathway is a signaling pathway for interferon, and many other cytokines involved in immune regulation. And TNF signaling pathway is associated with tumor necrosis factor signaling, which plays an important role in the immune response. The heat map demonstrates the upregulation of genes such as heat shock 70 kDa protein 6 (HSPA6), heat shock 70 kDa protein 1A (HSPA1A), heat shock 70 kDa protein 1B (HSPA1B) (Figure 4D). The HSPA6, HSPA1A, and HSPA1B genes belong to members of the heat shock protein heat shock protein 70 (HSP70) family, which is involved in the survival and function of immune cells, particularly in response to stress and protein folding.[37] HSP70, whether situated on the cancer cell membrane or secreted into the extracellular milieu, has the potential to trigger anti-tumor immune responses.[38–40] Under the influence of microwave heating, HSP70 protein induces the activation of $CD4^+$ and $CD8^+$ T cells mediated by DCs.[41,42] In the protein-protein interaction network, the nodes of interleukin-21 receptor (IL21R), HSPA6, HSPA1A, HSPA1B, and HSPH1 genes related to immune activation were larger, indicating their importance in the network (Figure 4E). Figure 4F shows the network relationship of gene protein interactions involved in the five immune-related pathways (shown in Figure 4C), in which HSPA6, HSPA1A, HSPA1B and other genes play an important role in the maturation of B cells, dendritic cells, and the cytokines IFN-γ and TNF-α. Therefore, these genes reveal the UPS nanoparticle mediated PTT can activate immune-related genes and promote dendritic cells to mature as antigens, further activating the immune system. It is well known that the 808-nanometer near-infrared laser has limited penetration ability and cannot deeply penetrate the human body. Thus, solely in terms of penetration capability, there are limitations in using UPS nanoparticles for intense treatment of internal tumors. However, RNA sequencing analysis indicates that, at the genetic level, PTT mediated by UPS nanoparticles can trigger immune-related pathways and antigens. This discovery holds significant relevance for enhancing the immune microenvironment infiltration within tumors.

Biocompatibility Assessment of UPS Nanoparticle in Cellular and Animal Models

Biocompatibility is a critical factor in the field of nanomedicine, especially when considering their applications in biomedicine and clinical translation. The established FDA-approved status of ultrasmall superparamagnetic iron oxide (USPIO) further confirms its positive biocompatibility. In this study, our primary objective was to thoroughly assess the biocompatibility of UPS nanoparticles. To achieve this, we conducted a series of comprehensive evaluations, including in vitro hemolysis assays, in vivo body weight assessments, blood tests, and tissue histopathology.

The role of UPS nanoparticle surface hydrophobicity on hemolytic behavior was established by incubating UPS nanoparticles ranging from 0 to 200 μg mL^{-1} with red blood cells (RBCs) (Figure 5A). The dosage of 200 μg mL^{-1} UPS nanoparticles exhibited negligible hemolytic activity. This outcome demonstrates that the UPS nanoparticles had minimal detrimental effects on RBCs even at 200 μg mL^{-1} concentration, which is relevant for in vivo applications. After intravenous administration of UPS nanoparticles, the weight change of mice during the treatment period was monitored. No weight loss of mice further confirmed none any severe systemic toxicity caused by UPS nanoparticles during the course of the study (Figure 5B). Furthermore, the results from blood routine tests (Figure 5C) and blood biochemistry tests (Figure 5D) demonstrated no discernible differences between groups that were injected with UPS nanoparticles and those administered physiological saline. This outcome also underscores the notable lack of toxicity associated with these nanoparticles at the tested doses, providing additional evidence of their biocompatibility. And the H&E staining conducted on major organs offered a critical assessment of potential organ damage stemming from UPS nanoparticles

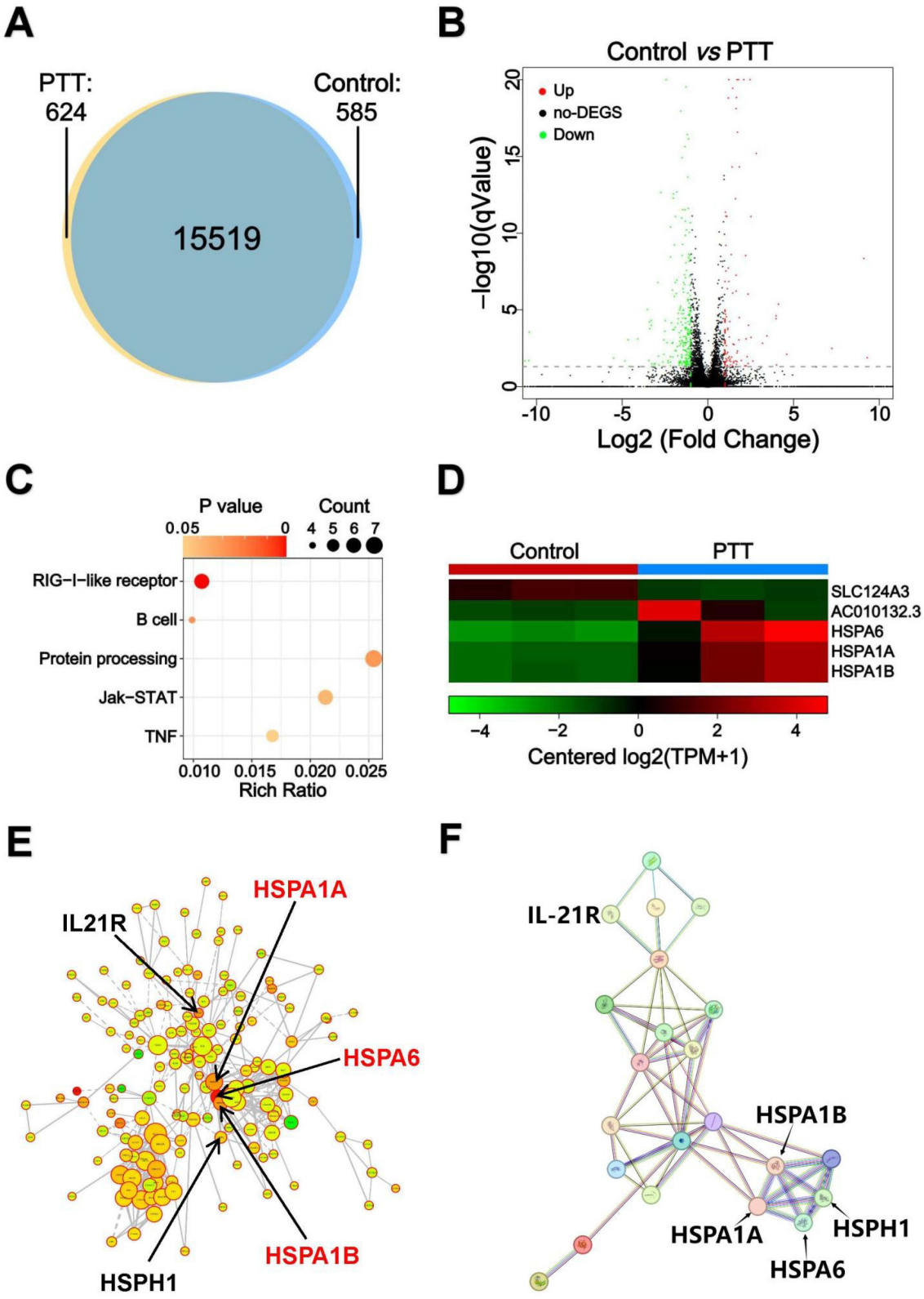

Figure 4 Transcription analysis of human nasopharyngeal carcinoma cells treated with 200 μg mL^{-1} UPS nanoparticles under 808 nm laser (2.1 W cm^{-2}) irradiation by RNA-sequencing. (**A**) A Venn diagram was used to illustrate the gene transcription patterns within each treatment group. (**B**) Volcano plots were utilized to visualize the genes with differential expression, while the absence of differentially expressed genes was labeled as no-DEGs. (**C**) The analysis of kyoto encyclopedia of genes and genomes (KEGG) pathways demonstrated the activation of immune-related pathways due to PTT. (**D**) The heat map visualizes genes exhibiting differential expression. (**E**) Networks depicting protein-protein interactions were constructed. The red text all belong to the family of heat shock proteins. (**F**) The network relationships of gene protein interactions involved in immune-related pathways.

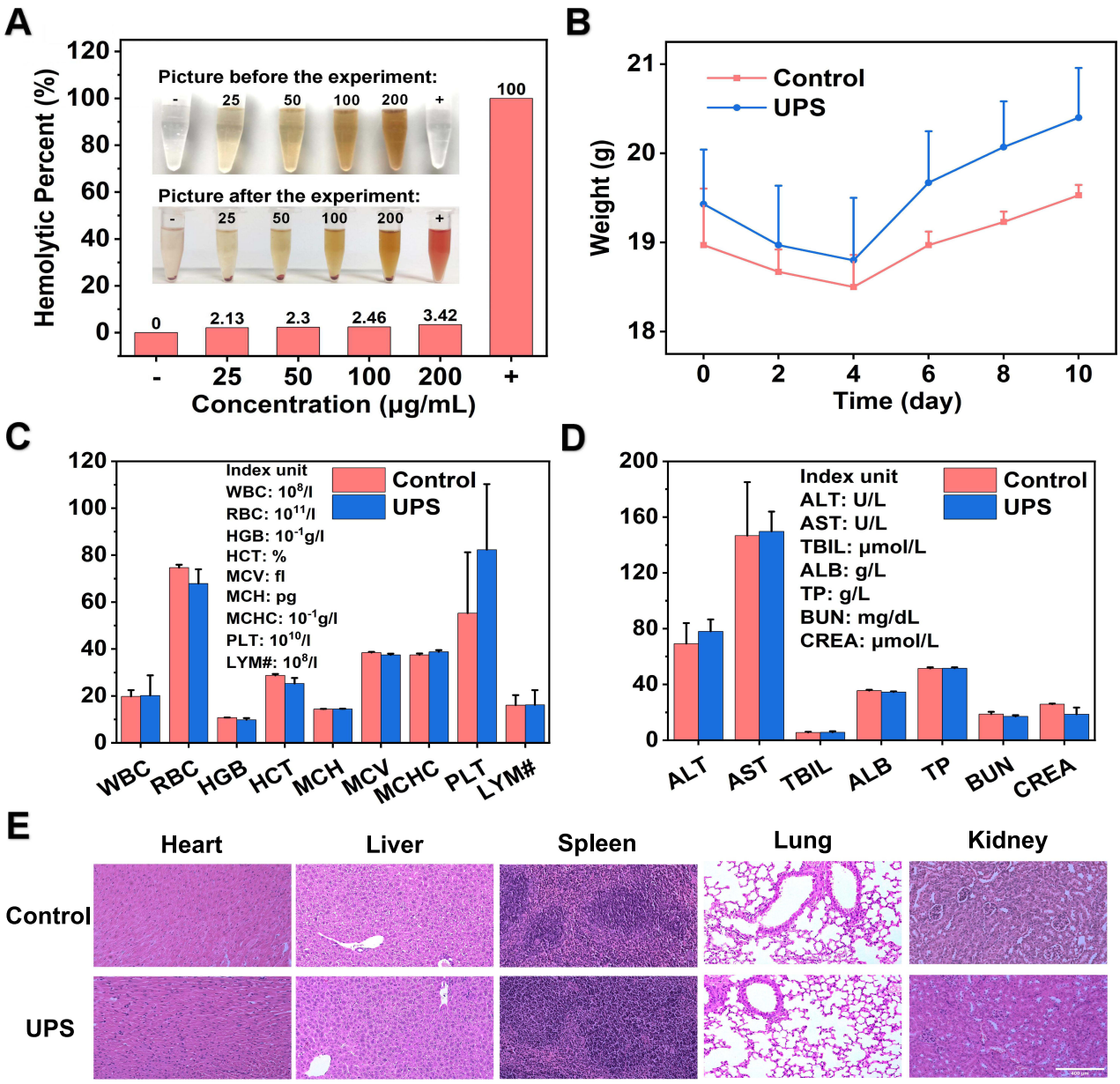

Figure 5 In vitro hemolysis analysis and in vivo systemic toxicity analysis. (**A**) Hemolysis analysis conducted in solutions with concentrations of UPS nanoparticles ranging from 0 to 200 μg mL^{-1}. (**B**) After intravenous administration of UPS nanoparticles or physiological saline (the control group) to mice, alterations in mouse body weight were assessed. Results are depicted as the mean ± standard error of the mean (SEM) (n = 3). (**C**) Blood routine analysis was performed, and the results are presented as mean ± standard error (n = 3). The # symbol represents the absolute value. (**D**) Blood biochemical analysis of ALT, AST, TBIL, ALB, TP, BUN and CREA. Results are depicted as the mean ± SEM (n = 3). (**E**) Hematoxylin and eosin (H&E) staining of the heart, liver, spleen, lung, and kidney in the control group and UPS group (scale bar: 400 μm).

(Figure 5E). Importantly, no significant indications of organ damage were observed. This comprehensive examination of major organs provides valuable insights into the potential systemic effects of the UPS nanoparticles, supporting their biocompatibility.

In vivo Pharmacokinetics and Photothermal Properties of UPS Nanoparticle

In vivo therapeutic effects of photothermal therapy enhancing aPD-L1 immunotherapy of UPS nanoparticle were subsequently evaluated in the animal groups with different treatments (aPD-L1 alone, PTT mediated by UPS nanoparticles, integration of photothermal therapy mediated by UPS nanoparticles and aPD-L1, with PBS as a control) (Figure 6A). To investigate the in vivo pharmacokinetics of UPS nanoparticles, we employed ICP-OES to quantify

iron (Fe) levels within the samples. Temporal evaluation revealed a decrease in Fe concentration over time (Figure 6B). And the half-life was calculated to be 1.82 ± 0.34 h. This outcome offers insight into the kinetics of nanoparticle clearance from the bloodstream, a critical aspect when considering their clinical feasibility. And the exceptional photothermal performance in vitro of UPS nanoparticles prompted us to investigate their utility for in vivo infrared thermal imaging (Figure 6C). As time elapsed, the thermal imaging of the tumor site in mice injected with UPS nanoparticles exhibited a significant enhanced red glow. These results suggest the potential of UPS nanoparticles as

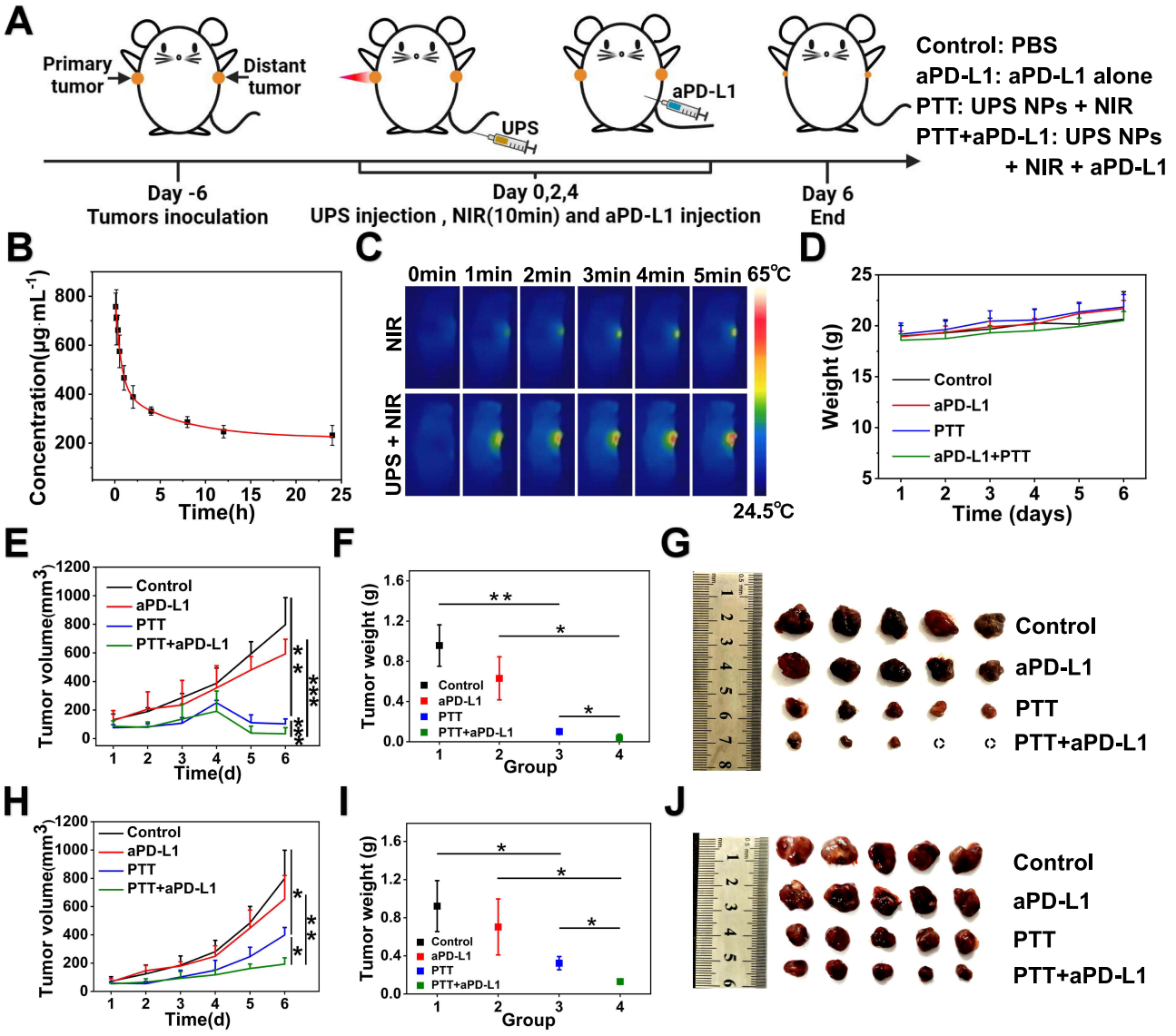

Figure 6 In vivo pharmacokinetics and the photothermal effect enhancing aPD-L1 immunotherapy of UPS nanoparticle. (**A**) Schematic illustration of the integration of photothermal therapy mediated by UPS nanoparticles and aPD-L1 immune checkpoint blockade therapy in male C57BL/6J mice to suppress primary and distant metastatic tumors. The experimental groups of this therapeutic approach have different treatment settings. UPS nanoparticles were injected every 2 days for PTT group and PTT+aPD-L1 group. The 808 nm laser irradiation was applied for 10 min for these two groups. For PTT+aPD-L1 group, UPS nanoparticles were injected once, followed by laser irradiation and the injection of aPD-L1 once. For control group and aPD-L1 group, the PBS and aPD-L1 were injected every 2 days, respectively. (**B**) Blood circulation time of administered 300 μL of 1 mg mL^{-1} UPS nanoparticles aqueous solution determined by inductively coupled plasma optical emission spectroscopy (ICP-OES). (**C**) Infrared thermal imaging corresponding to NIR laser irradiation alone and NIR laser irradiation with UPS nanoparticles. (**D**) Alterations in weight change of mice following diverse treatment regimens. (**E**) Primary tumor growth inhibition curves after treatment of mice with aPD-L1 alone, PTT mediated by UPS nanoparticles, and integration of photothermal therapy mediated by UPS nanoparticles and aPD-L1, with phosphate-buffered saline (PBS) as a control. (**F**) Primary tumors weight collected after the mice were sacrificed. (**G**) Photographs of the primary tumors in the 4 mouse groups post different interventions. (**H**) Distant metastatic tumor growth inhibition curves after treatment of mice with aPD-L1 alone, PTT mediated by UPS nanoparticles, and integration of photothermal therapy mediated by UPS nanoparticles and aPD-L1, with PBS as a control. (**I**) Distant metastatic tumor weights collected after the mice were sacrificed. (**J**) Photographs of the distant metastatic tumors in the 4 mouse groups post different interventions.

Notes: *Representing $p < 0.05$, **$p < 0.01$, and ***$p < 0.001$, based on a sample size of $n = 5$.

effective contrast agents for infrared photothermal imaging. This capability of UPS nanoparticles enables real-time thermodynamic monitoring during PTT, providing a valuable tool to clinical application. Furthermore, mice injected with UPS nanoparticles and subjected to 808 nm laser irradiation achieved a tumor temperature increase to nearly 65 °C within 5 minutes, compared to tumors subjected to laser irradiation alone. This temperature is sufficient to kill tumor cells, confirming the in vivo outstanding photothermal conversion capability of UPS nanoparticles.

UPS Nanoparticle-Mediated PTT Enhances the Therapeutic Efficacy of aPD-L1 in vivo

Immunotherapy is a major strategy of antitumor therapy, whereas it still faces many challenges in clinical application. Although a large number of studies have revealed numerous mechanisms for the occurrence of immunotherapy resistance, it is still the tip of the iceberg in the face within the intricate tumor immune microenvironment, especially head and neck squamous cell carcinoma.[43,44] Here, we established a bilateral squamous cell carcinoma 7 (SCC7) subcutaneous tumor model to simulate the process of cancer metastasis. The timeline of the animal experiments is depicted in Figure 6A. Remarkably, mice in different experimental groups did not exhibit significant weight loss throughout the treatment period (Figure 6D). These results indicate that the treatments were generally well-tolerated by the mice and hardly induced systemic toxicity in mice. The growth trend graphs of primary tumor volume and distant tumor volume are shown in Figure 6E and H, respectively. As the treatment days progressed, the tumor volume in the PBS control group and aPD-L1 alone group increased rapidly, while the UPS nanoparticles mediated PTT group exhibited slower tumor volume growth, and the PTT+aPD-L1 group showed the slowest growth. Following the treatment procedures, all mice were euthanized, and their respective tumors were excised and quantified by weight. The weights of both primary and distant tumors in the PTT+aPD-L1 group were significantly lighter than the other three groups, followed by the PTT group, while the control group and aPD-L1 group had the highest tumor weights (Figure 6F and I). And the anatomical images assessed the size of the primary tumors (Figure 6G) and distant tumors (Figure 6J). In these images, the PTT+aPD-L1 group displayed the smallest tumor size, even complete disappearance, significantly outperforming the outcomes of aPD-L1 or PTT monotherapies. Therefore, all these results indicate that UPS nanoparticles mediated PTT can significantly enhance the therapeutic efficacy of aPD-L1, whereas aPD-L1 monotherapy is much less effective.

And the results of the primary tumors H&E staining (Figure 7A) are consistence with the above conclusions. It revealed that the control group and the aPD-L1 group caused the least amount of cellular apoptotic damage, while the PTT group exhibited an increased number of apoptotic cells, and the PTT+aPD-L1 group induced the highest level of cellular apoptosis. However, the H&E staining conducted on major organs offered a critical assessment of potential organ damage stemming after several therapeutic treatments, and no significant indications of organ damage were observed in the PTT+aPD-L1 group (Figure 7B). This comprehensive examination of major organs provides valuable insights into the potential systemic effects after the PTT enhancing aPD-L1 immunotherapy, supporting the biocompatibility of this therapeutic treatment.

In vivo Activation of the Antitumor Immune Response of PTT Enhancing aPD-L1 Immunotherapy

In order to detect the tumor cells proliferation after therapy, the Ki67 IHC staining (Figure 8A) was assessed. It showed that Ki67 expression was the lowest in the PTT+aPD-L1 groups, followed by the PTT group, and the highest in the control group and aPD-L1 group. These results demonstrate that the PTT+aPD-L1 groups had the slowest tumor growth rate and mitotic rate, comparing with the faster tumor growth and mitotic rate of the aPD-L1 group, which was Ki67-sensitive, with more brown tissues. Therefore, after UPS nanoparticles mediated PTT enhancing aPD-L1 immunotherapy, the tumor sites of prognosis may have not recurrence.

To elucidate the in-depth mechanisms underlying the antimetastatic effectiveness arising from the UPS nanoparticles mediated PTT enhancing aPD-L1 immunotherapy, the immunofluorescence staining experiments for CRT and HMGB1 protein expression were assessed (Figure 8B–E). When ICD occurs in tumor cells, CRT will be exposed onto the cellular membrane surface and act as an “eat-me” signal to promote DCs or its precursor cells to phagocytic dead or dying tumor

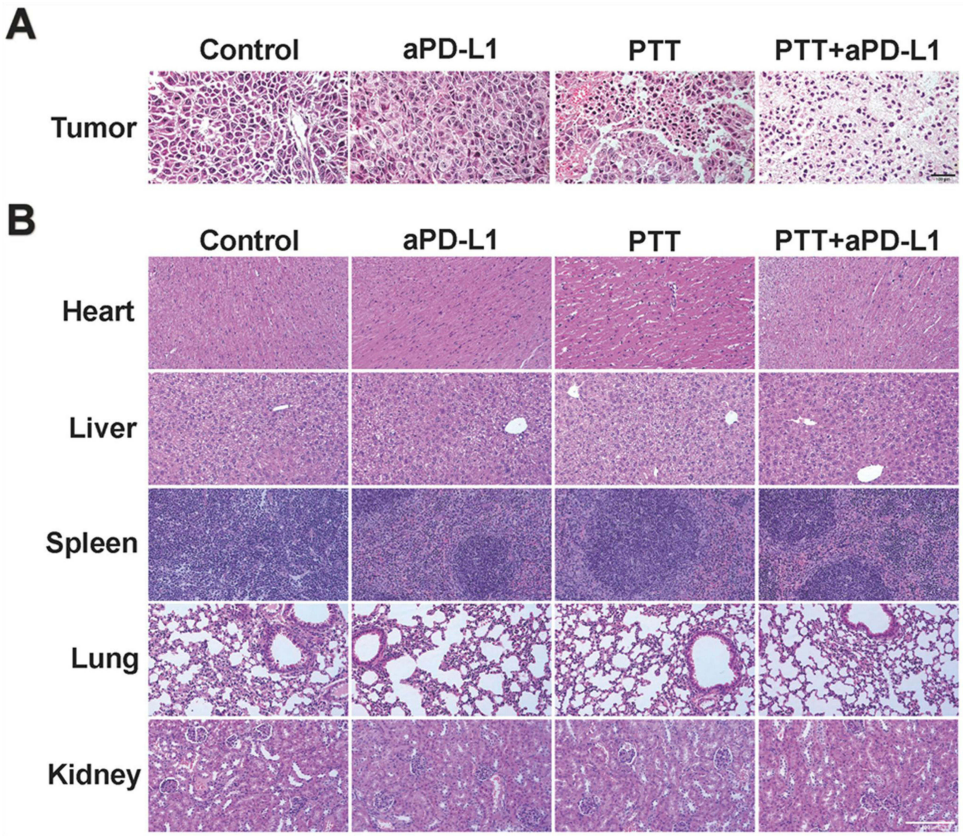

Figure 7 The images of H&E staining about the primary tumor tissues. (**A**) H&E staining of primary tumors. Scale bars represent 100 μm. (**B**) Histological analysis of vital organs across distinct treatment categories. Scale bars represent 400 μm.

cells, thereby furnishing abundant antigenic materials to stimulate dendritic cell maturation and facilitate their functional activation;[45] and the HMGB1 released extracellular can activate the corresponding signaling pathway and activate immunity.[46] The PTT+aPD-L1 groups exhibited the strongest fluorescence on the tumor cell membranes. The average fluorescence intensity of CRT in the PTT+aPD-L1 group was 2.34 times higher than that of the PTT group, while there was no fluorescence in the control and aPD-L1 groups. And the average fluorescence intensity of HMGB1 in the PTT +aPD-L1 group was 1.51 times higher than that of the PTT group, while there was no fluorescence in the control and aPD-L1 groups. These results imply that UPS nanoparticle-based PTT enhancing aPD-L1 immunotherapy triggered more ICD in tumor cells and effectively promoted CRT and HMGB1 protein expression of tumors.

The intratumoral infiltration of T lymphocytes, including cytotoxic T lymphocytes CTLs (CD8) and T helper cells (CD4) was also investigated by the immunofluorescence staining (Figure 9A–C). The average fluorescence intensity of $CD8^+$ T cells in the PTT+aPD-L1 group was 14.79 times higher than that of the aPD-L1 group. And the average fluorescence intensity of $CD4^+$ T cells in the PTT+aPD-L1 group was 14.46 times higher than that in the aPD-L1 group. These results demonstrate that UPS nanoparticle-based PTT significantly stimulated the proliferation of $CD8^+$ and $CD4^+$ T cells and effectively strengthened T-cell infiltration of tumors, improving the tumor microenvironment that was in a suppressed state when aPD-L1 was used alone, greatly enhancing the therapeutic efficacy of aPD-L1.

Furthermore, the levels of tumor necrosis factor-alpha (TNF-α) and interferon-gamma (IFN-γ) secreted by spleen cells in the PTT+aPD-L1 groups were also assessed, which were significantly elevated (Figure 9D and E). The pro-inflammatory cytokine TNF-α belongs to the TNF ligand superfamily and exhibits pleiotropic pro-inflammatory properties.[47] TNF-α serves diverse functions in modulating immune processes, encompassing inflammation, cellular differentiation, lipid metabolism, and programmed cell death. IFN-γ or type II interferon plays a crucial role in innate and adaptive immunity against viral pathogens, bacterials, and protozoal infections.[48] Aside from its direct role in suppressing viral replication, IFN-γ's significance within the immune system is further evident through its functions in immune

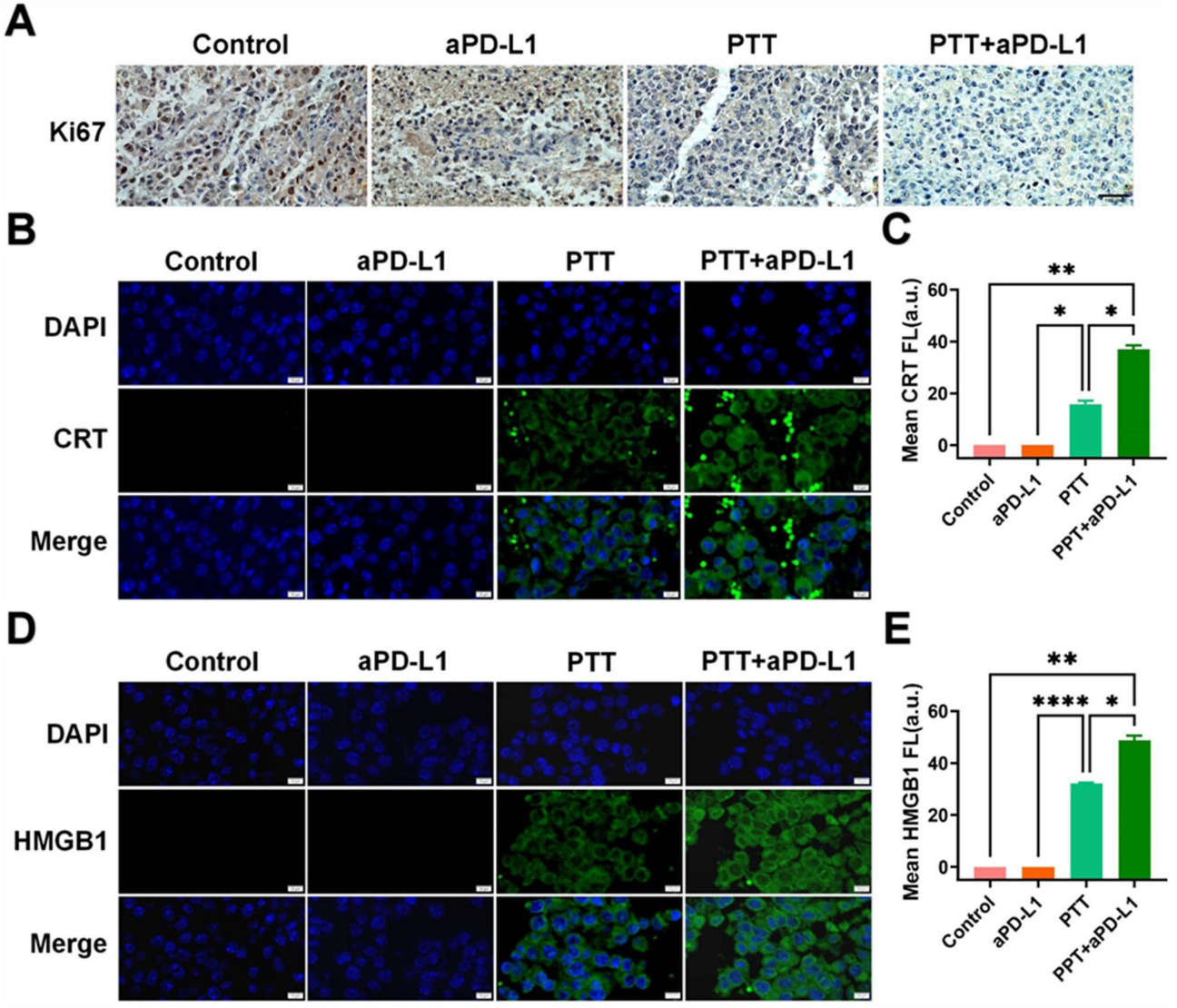

Figure 8 The images of immunohistochemical (IHC) staining assessing Ki67 expression and immunofluorescence analysis of CRT and HMGB1 about the primary tumor tissues. (**A**) IHC staining assessing Ki67 expression of the tumor cells proliferation. Scale bars represent 100 μm. (**B**) Immunofluorescence analysis of calreticulin (CRT) expression from primary tumor tissues of the four different groups (scale bar: 10 μm). (**C**) Fluorescence quantitative fluorescence analysis of CRT. (**D**) Immunofluorescence analysis of high mobility group box-1 protein (HMGB1) expression from primary tumor tissues of the four different groups (scale bar: 10 μm). (**E**) Quantitative fluorescence analysis of HMGB1. Three randomly chosen visual fields were evaluated for histological quantification. Data are represented as mean ± SD.
Notes: The asterisks indicate statistical significance levels, with *Representing $p < 0.05$, **$p < 0.01$, and ****$p < 0.0001$, based on a sample size of n = 3.

enhancement and immune regulation. The TNF-α level in the blood of the PTT+aPD-L1 group were 3.03 times higher than those in the aPD-L1 group. The IFN-γ levels in the blood of the PTT+aPD-L1 group were 3.39 times higher than those in the aPD-L1 group. These results highlight the ability of PTT mediated by UPS nanoparticles enhancing aPD-L1 immunotherapy to trigger a stronger systemic immune response through the secretion of cytokines by $CD4^+$ T cells for anti-tumor activity than that of aPD-L1 alone.

To assess the apoptosis levels of tumors in various groups, terminal deoxynucleotidyl transferase dUTP nick end labeling (TUNEL) immunofluorescence staining was investigated (Figure 10A and B). The PTT+aPD-L1 groups exhibited the strongest fluorescence on the apoptosis of tumors. And PTT+aPD-L1 group exhibited the highest apoptotic rate, which was 7.05 times higher than that of aPD-L1 group. This result demonstrates that under the UPS-mediated PTT, the treatment effect with aPD-L1 can be effectively enhanced, resulting in the induction of the optimal degree of apoptotic damage. Furthermore, in order to detect the tumor cell proliferation state after several treatments, the Proliferating cell nuclear antigen (PCNA) immunofluorescence staining experiments were assessed (Figure 10C and D). The more robust proliferative activity of tumor

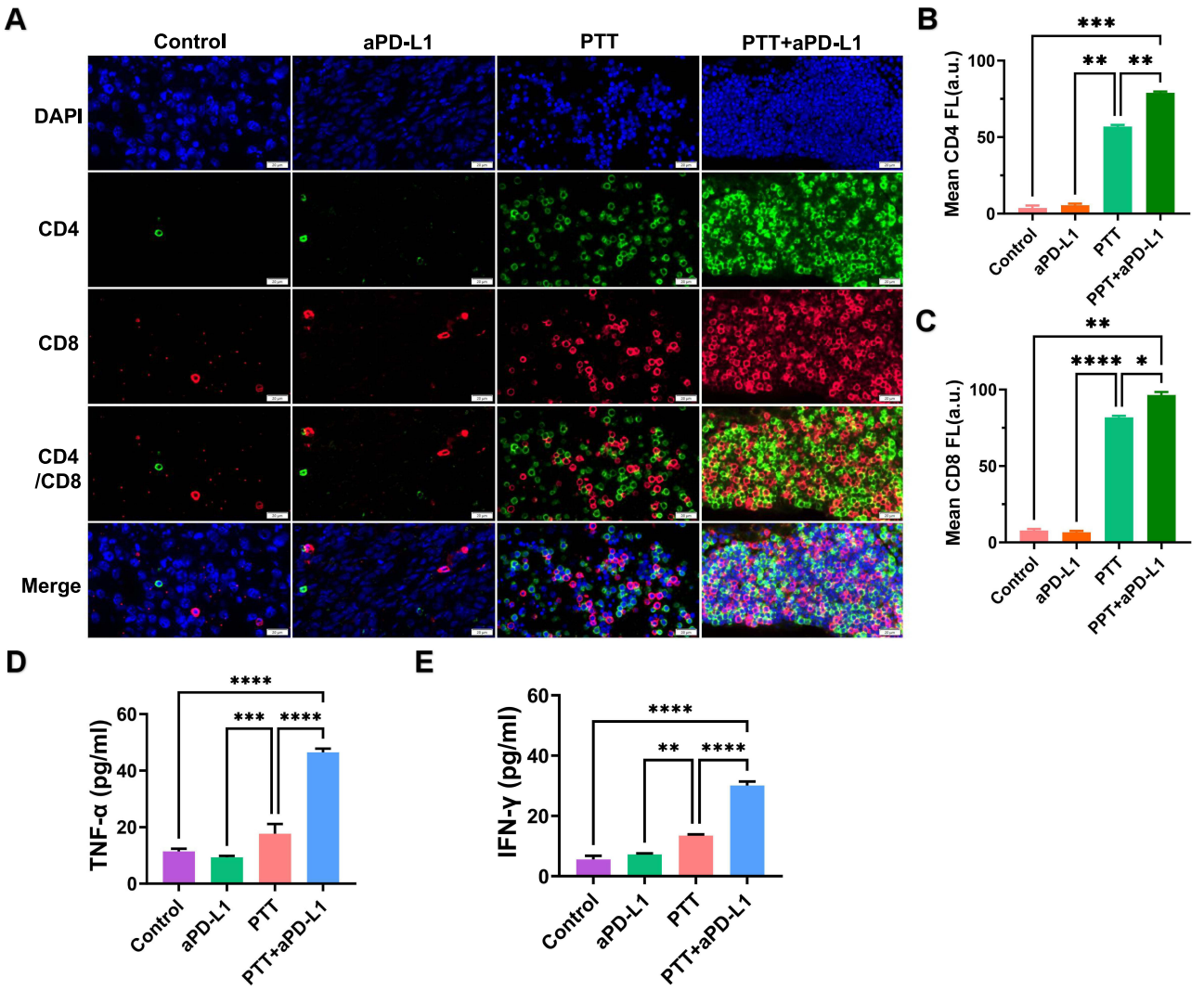

Figure 9 The immunofluorescence analysis of $CD4^+$ and $CD8^+$ T lymphocytes and concentration quantification of the cytokines about the distant tumor tissues. (**A**) Immunofluorescence illustrations depicting the proliferation of $CD4^+$ and $CD8^+$ T lymphocytes within distant tumor tissues across the four distinct groups following various treatments (scale bar: 20 μm). (**B**) Quantitative fluorescence analysis of $CD4^+$ T lymphocytes. Three randomly chosen visual fields were evaluated for histological quantification. (**C**) Quantitative fluorescence analysis of $CD8^+$ T lymphocytes. (**D**) Quantification of concentrations of the cytokines TNF-α in the blood serum of mice within different experimental groups. (**E**) Quantification of concentrations of the cytokines IFN-γ. Data are represented as mean ± SD.
Notes: The asterisks indicate statistical significance levels, with *Representing $p < 0.05$, **$p < 0.01$, ***$p < 0.001$, and ****$p < 0.0001$, based on a sample size of $n = 3$.

cells, the higher the fluorescence intensity of PCNA, which serves as an indicator for assessing tumor cellular proliferation status. These results revealed the gradual decrease in PCNA expression levels in all groups, with the lowest levels in the PTT +aPD-L1 treatment group, which had the almost negligible fluorescence intensity of PCNA. And in the aPD-L1 group, PCNA expression was 14.92 times higher than that of the PTT+aPD-L1 treatment group. This result indicates that UPS-mediated PTT effectively enhances the inhibitory effect on tumor cells proliferation in the aPD-L1 treatment group.

Mechanism of UPS Nanoparticle Mediated PTT Enhancing aPD-L1 Immunotherapy

The rationale behind the aforementioned findings could be attributed to the inclusion of UPS nanoparticle mediated PTT to aPD-L1 immunotherapy can potentiate the immune response within the body to suppress the recurrence and metastasis of tumor cells, and also promote the antitumor therapeutic effect. When using aPD-L1 immune checkpoint inhibitors alone, the tumor microenvironment of HNSCC is in an immunosuppressive state, resulting in a low number of immune cells. Even if aPD-L1 recognizes the PD-L1 on cancer cells, there is limited immune cell infiltration. Consequently, the efficacy of aPD-L1 monotherapy is quite poor. However, when the UPS nanotheranostic agent with excellent

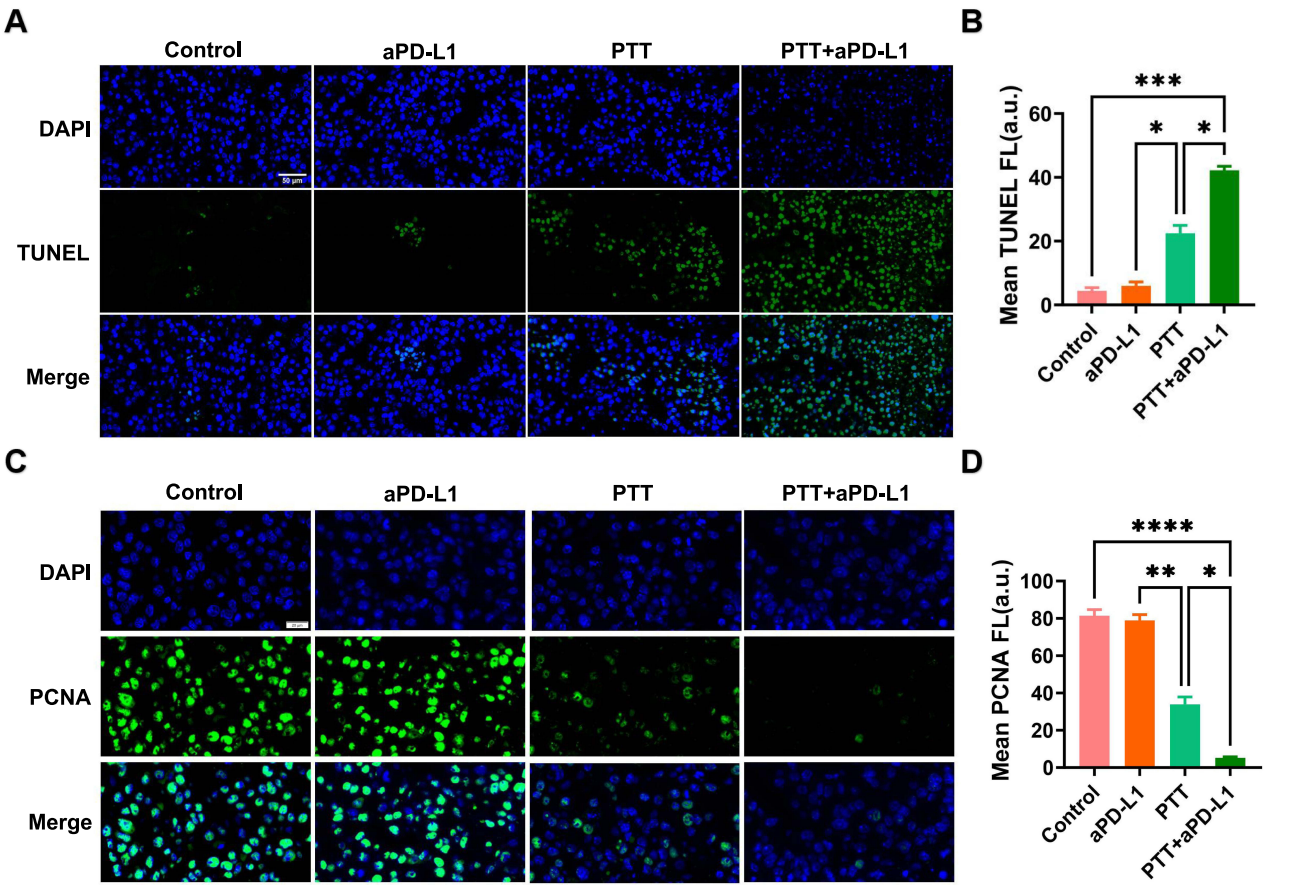

Figure 10 The immunofluorescence staining of TUNEL and PCNA to detect the apoptosis level and proliferative activity of distant tumors. (**A**) Immunofluorescent labeling targeting TUNEL was performed on distant tumors (scale bar: 50 μm). (**B**) Quantitative fluorescence analysis of TUNEL. (**C**) Proliferating cell nuclear antigen (PCNA) staining was conducted on distant tumors (scale bar: 20 μm). (**D**) Quantitative fluorescence analysis of PCNA. Three randomly chosen visual fields were evaluated for histological quantification. The data are presented as the mean ± standard deviation.
Notes: The asterisks indicate statistical significance levels, with *Representing $p < 0.05$, **$p < 0.01$, ***$p < 0.001$, and ****$p < 0.0001$, based on a sample size of $n = 3$.

biocompatibility is intravenously injected into mice, the sialyl Lewis X targeting moiety of UPS nanoparticles can effectively target the tumor sites. Via the targeting effect of sialyl Lewis X targeting molecules, combined with enhanced permeability, these can effectively increase the UPS nanoparticles uptake of tumor cells with immunotherapy resistance. And the UPS nanoparticles can produce hyperthermia (temperature can reach nearly 65 °C) of PTT effect under 808 nm laser irradiation. PTT can lead to the localized primary tumor cells death, releasing a series of abundant immunogenic signaling molecules such as CRT and HMGB1. These molecules can be recognized by the body's immune system, activating immune cells. And the dying tumor cells display the "Eat me" signal on their surface and are recognized by phagocytes. Then the phagocytes swallow tumor cell fragments, promote the maturation of DCs, stimulate T cell antigen receptors, cause a substantial proliferation of $CD4^+$ and $CD8^+$ T cells, and increase the effect of $CD4^+$ T and $CD8^+$ T cells infiltration. And the activating CTLs arrive at the systemic tumor site, where aPD-L1 binds to PD-L1 on cancer cells. The binding effect can prevent cancer cells from recognizing CTLs, thereby preserving the activity of CTLs and significantly enhancing their ability to eliminate tumor cells. Finally, CTLs can kill the distant metastatic tumor cells. Furthermore, $CD4^+$ T cells possess the capacity to secrete the cytokines TNF-α and IFN-γ, exerting their influence systemically to reinforce the immune response, thereby impeding the recurrence and metastasis of tumor cells.

Conclusions

In summary, we reported the precision USPIO-PEG-SLe^x nanotheranostics agent targeted photothermal therapy for enhanced anti-PD-L1 immunotherapy to treat immunotherapy resistance. We have developed a versatile nano-diagnostic

and therapeutic platform, referred to as UPS, through an efficient amidation synthesis method. The acquired UPS nanoparticle exhibits excellent biocompatibility, strong dual-modal imaging capabilities (magnetic resonance imaging and thermal imaging), efficiently tumor-targeting properties, and the controllable ability to mediate photothermal therapy. At the genetic level, PTT mediated by UPS nanoparticles can trigger immune-related pathways (the RIG-I-like receptor signaling pathway, B cell receptor signaling pathway, protein processing in endoplasmic reticulum, Jak-STAT signaling pathway, and tumor necrosis factor (TNF) signaling pathway) and antigens. And the upregulation of gene is included the heat shock protein heat shock protein 70 (HSP70) family. Under the influence of microwave heating, HSP70 protein can induce the activation of $CD4^+$ and $CD8^+$ T cells mediated by DCs. The gene protein interactions involved in the five immune-related pathways, in which HSPA6, HSPA1A, HSPA1B and other genes play an important role in the maturation of B cells, dendritic cells, and the cytokines IFN-γ and TNF-α. PTT mediated by UPS nanoparticles can activate immune-related genes and promote dendritic cells to mature as antigens, further activating the immune system. This discovery in our work holds significant relevance for enhancing the immune microenvironment infiltration within tumors.

The efficacy of aPD-L1 monotherapy is quite poor, because of the immunosuppression state of the tumor microenvironment or limited immune cell infiltration. However, using the UPS nanotheranostic agent can effectively target the tumor sites via the targeting effect of sialyl Lewis X targeting molecules, and UPS nanoparticles can be effectively uptake of tumor cells with immunotherapy resistance. Then UPS nanotheranostic agent can produce hyperthermia under the 808 nm laser irradiation, leading to the eradication of primary tumors and subsequent induction of ICD and releasing a series of abundant immunogenic signaling molecules such as CRT and HMGB1. And the dying tumor cells display the "Eat me" signal on their surface and are recognized by phagocytes, whose can swallow tumor cell fragments, promote the maturation of DCs, stimulate T cell antigen receptors. Then ICD stimulation can significantly promote the proliferation of immune cells, increasing the numbers of $CD4^+$ T cells and $CD8^+$ T cells, as well as increasing the effect of $CD4^+$ T and $CD8^+$ T cells infiltration. And the activating CTLs arrive at the systemic tumor site, where aPD-L1 binds to PD-L1 on cancer cells. Finally, CTLs can kill the distant metastatic tumor cells. Furthermore, $CD4^+$ T cells can enhance the secretion of the cytokines TNF-α and IFN-γ to reinforce the immune response for impeding the tumor recurrence and metastasis. Therefore, the photothermal therapy mediated by UPS nanoparticles can assist the aPD-L1 treatment, thereby enhancing the effectiveness of immune checkpoint inhibitor immunotherapy, and achieving concurrent suppression of primary tumors and distant metastatic tumors. This work offers a facile, versatile, and rapid preparation multifunctional nanotheranostic agent to enhance the effectiveness of immune checkpoint inhibitor therapy with aPD-L1 to treat immunotherapy resistance, addressing the challenge of aPD-L1 treatment ineffectiveness in the development of nanomedicines, which holds the promise for clinical translation.

Abbreviations

aPD-L1, anti-Programmed Death-Ligand 1; USPIO-PEG, polyethylene glycol-coated ultrasmall superparamagnetic iron oxide; UPS, polyethylene glycol-coated ultrasmall superparamagnetic iron oxide nanoparticles coupled with sialyl Lewis X; ICP-OES, Inductively Coupled Plasma Optical Emission Spectroscopy; PTT, photothermal therapy; ROS, reactive oxygen species; ICB, immune checkpoint blockade; PD-L1, programmed death-ligand 1; PD-1, programmed cell death 1 receptor; mAb, monoclonal antibodies; FDA, Food and Drug Administration; ICD, immunogenic cell death; CRT, calreticulin; HMGB1, high mobility group box 1; PEG, Polyethylene glycol; HNSCC, head and neck squamous cell carcinoma; CTLs, cytotoxic T lymphocytes; SLe^x, Sialyl Lewis X; MES buffer, 2- (N-morpholino) ethanesulfonic acid buffer; EDC, 1-(3-dimethylaminopropyl)-3-ethylcarbodiimide; VSM, Vibration Sample Magnetometer; NIR, near-infrared; SCC7, squamous cell carcinoma 7; KEGG, kyoto encyclopedia of genes and genomes; ICP-OES, inductively coupled plasma optical emission spectroscopy; ELISA, Enzyme-linked immunosorbent assay; TNF-α, tumor necrosis factor-alpha; IFN-γ, interferon-gamma; TEM, transmission electron microscopy; Ms, saturation magnetization; NPs, nanoparticles; τ, time constant; η, photothermal conversion efficiency; MRI, magnetic resonance imaging; JC-1, mitochondrial membrane potential assay kit with JC-1; 0.1UPS, UPS nanoparticles aqueous solution with a concentration of 100 μg mL^{-1}; 0.2UPS, UPS nanoparticles aqueous solution with a concentration of 200 μg mL^{-1}; Cccp, carbonyl cyanide m-chlorophenyl hydrazone; TNF, tumor necrosis factor; HSPA6, heat shock 70 kDa protein 6; HSPA1A, heat shock 70 kDa

protein 1A; HSPA1B, heat shock 70 kDa protein 1B; HSP70, heat shock protein 70; DCs, dendritic cells; USPIO, ultrasmall superparamagnetic iron oxide; SEM, standard error of the mean; ALT, alanine aminotransferase; AST, aspartate aminotransferase; TBIL, total bilirubin; ALB, albumin; TP, total protein; BUN, blood urea nitrogen; CREA, creatinine; H&E, hematoxylin and eosin; RBCs, red blood cells; PBS, phosphate-buffered saline; IHC, immunohistochemical; TUNEL, terminal deoxynucleotidyl transferase dUTP nick end labeling; PCNA, proliferating cell nuclear antigen.

Ethics Approval and Consent to Participate

The ethical review of animal experiments adhered to the Guiding Opinions on the Humane Treatment of Laboratory Animals issued by the Ministry of Science and Technology of the People's Republic of China, as well as the National Standard GB/T35892-2018, titled Ethical Standards for Animal Welfare in Experimental Research. It was approved by the Animal Experiment Ethics Committee of the Affiliated Tumor Hospital of Guangxi Medical University.

Consent for Publication

All authors give consent for the publication of the manuscript in International Journal of Nanomedicine.

Funding

Financial support for this study was provided by the Natural Science Foundation of Guangxi Province (2018GXNSFAA281095), the Guangxi Clinical Research Center for Medical Imaging Construction (Grant No. Guike AD20238096), and Guangxi Health Commission Key Laboratory of Tumor Molecular Imaging (Guangxi Medical University Cancer Hospital, Grant No. ZPZH2020004).

Disclosure

The authors declare no competing interests for this work.

References

1. Sung H, Ferlay J, Siegel RL, et al. Global cancer statistics 2020: GLOBOCAN estimates of incidence and mortality worldwide for 36 cancers in 185 countries. *CA Cancer J Clin*. 2021;71:209–249.
2. Walia V, Kaushik D, Mittal V, et al. Delineation of neuroprotective effects and possible benefits of antioxidants therapy for the treatment of Alzheimer's diseases by targeting mitochondrial-derived reactive oxygen species: bench to bedside. *Mol Neurobiol*. 2022;59:657–680. doi:10.1007/s12035-021-02617-1
3. Li J, Wei D, Fu Q. Anatase TiO2− x and zwitterionic porphyrin polymer-based nanocomposite for enhanced cancer photodynamic therapy. *Nanoscale*. 2023;15(36):14790–14799. doi:10.1039/D3NR03012A
4. Sun K, Yuan L, Chen S, Sun Y, Wei D. Alendronate Pt^{IV} prodrug amphiphile for enhanced chemotherapy targeting and bone destruction inhibition in osteosarcoma. *Adv Healthc Mater*. 2023;e2302746. doi:10.1002/adhm.202302746
5. Verma R, Kaushik D. *In vitro* lipolysis as a tool for the establishment of IVIVC for lipid-based drug delivery systems. *Curr Drug Deliv*. 2019;16(8):688–697. doi:10.2174/1567201816666190620115716
6. Cohen EEW, Bell RB, Bifulco CB, et al. The society for immunotherapy of cancer consensus statement on immunotherapy for the treatment of squamous cell carcinoma of the head and neck (HNSCC). *J Immunother Cancer*. 2019;7:184. doi:10.1186/s40425-019-0662-5
7. Yi M, Zheng X, Niu M, Zhu S, Ge H, Wu K. Combination strategies with PD-1/PD-L1 blockade: current advances and future directions. *Mol Cancer*. 2022;21:28. doi:10.1186/s12943-021-01489-2
8. Akinboro O, Larkins E, Pai-Scherf LH, et al. FDA approval summary: pembrolizumab, atezolizumab, and cemiplimab-rwlc as single agents for first-line treatment of advanced/metastatic PD-L1-high NSCLC. *Clin Cancer Res*. 2022;28:2221–2228. doi:10.1158/1078-0432.CCR-21-3844
9. Suzman DL, Agrawal S, Ning YM, et al. FDA approval summary: atezolizumab or pembrolizumab for the treatment of patients with advanced urothelial carcinoma ineligible for cisplatin-containing chemotherapy. *Oncologist*. 2019;24:563–569. doi:10.1634/theoncologist.2018-0084
10. Jiang Y, Zhao X, Fu J, Wang H. Progress and challenges in precise treatment of tumors with PD-1/PD-L1 blockade. *Front Immunol*. 2020;11:339. doi:10.3389/fimmu.2020.00339
11. Oliva M, Spreafico A, Taberna M, et al. Immune biomarkers of response to immune-checkpoint inhibitors in head and neck squamous cell carcinoma. *Ann Oncol*. 2019;30(1):57–67. doi:10.1093/annonc/mdy507
12. Saada-Bouzid E, Defaucheux C, Karabajakian A, et al. Hyperprogression during anti-PD-1/PD-L1 therapy in patients with recurrent and/or metastatic head and neck squamous cell carcinoma. *Ann Oncol*. 2017;28(7):1605–1611. doi:10.1093/annonc/mdx178
13. Garralda E, Laurie SA, Seymour L, de Vries EGE. Towards evidence-based response criteria for cancer immunotherapy. *Nat Commun*. 2023;14. doi:10.1038/s41467-022-35215-3
14. Wang M, Rousseau B, Qiu K, et al. Killing tumor-associated bacteria with a liposomal antibiotic generates neoantigens that induce anti-tumor immune responses. *Nat Biotechnol*. 2023. doi:10.1038/s41587-023-01957-8

15. Yang B, Liu T, Qu Y, et al. Progresses and perspectives of anti-PD-1/PD-L1 antibody therapy in head and neck cancers. *Front Oncol*. 2018;8:563. doi:10.3389/fonc.2018.00563
16. Wu M, Huang Q, Xie Y, et al. Improvement of the anticancer efficacy of PD-1/PD-L1 blockade via combination therapy and PD-L1 regulation. *J Hematol Oncol*. 2022;15:24. doi:10.1186/s13045-022-01242-2
17. Liu L, Huang X, Shi F, et al. Combination therapy for pancreatic cancer: anti-PD-(L)1-based strategy. *J Exp Clin Cancer Res*. 2022:41. doi:10.1186/s13046-022-02244-1
18. Yin S, Chen Z, Chen D, Yan D. Strategies targeting PD-L1 expression and associated opportunities for cancer combination therapy. *Theranostics*. 2023;13:1520–1544. doi:10.7150/thno.80091
19. Zhang Y, Dong P, Yang L. The role of nanotherapy in head and neck squamous cell carcinoma by targeting tumor microenvironment. *Front Immunol*. 2023;14:1189323. doi:10.3389/fimmu.2023.1189323
20. Verma R, Mittal V, Pandey P, et al. Exploring the role of self-nanoemulsifying systems in drug delivery: challenges, issues, applications and recent advances. *Curr Drug Deliv*. 2023;20:1241–1261. doi:10.2174/1567201819666220519125003
21. Verma R, Kaushik A, Almeer R, Rahman MH, Abdel-Daim MM, Kaushik D. Improved pharmacodynamic potential of rosuvastatin by self-nanoemulsifying drug delivery system: an *in vitro* and *in vivo* evaluation. *Int J Nanomed*. 2021;16:905–924. doi:10.2147/IJN.S287665
22. Xu M, Zhang C, He S, Xu C, Wei X, Pu K. Activatable immunoprotease nanorestimulator for second near-infrared photothermal immunotherapy of cancer. *ACS Nano*. 2023;17:8183–8194. doi:10.1021/acsnano.2c12066
23. Huang X, Lu Y, Guo M, Du S, Han N. Recent strategies for nano-based PTT combined with immunotherapy: from a biomaterial point of view. *Theranostics*. 2021;11(15):7546–7569. doi:10.7150/thno.56482
24. Zhao Y, Liu X, Liu X, et al. Combination of phototherapy with immune checkpoint blockade: theory and practice in cancer. *Front Immunol*. 2022;13:955920. doi:10.3389/fimmu.2022.955920
25. Chang M, Hou Z, Wang M, Li C, Lin J. Recent advances in hyperthermia therapy-based synergistic immunotherapy. *Adv Mater*. 2021;33(4):e2004788. doi:10.1002/adma.202004788
26. Tang H, Xu X, Chen Y, et al. Reprogramming the tumor microenvironment through second-near-infrared-window photothermal genome editing of PD-L1 mediated by supramolecular gold nanorods for enhanced cancer immunotherapy. *Adv Mater*. 2021;33(12):e2006003. doi:10.1002/adma.202006003
27. Fang X, Wu X, Li Z, et al. Biomimetic anti-PD-1 peptide-loaded 2D FePSe(3) nanosheets for efficient photothermal and enhanced immune therapy with multimodal MR/PA/thermal imaging. *Adv Sci*. 2021;8(2):2003041. doi:10.1002/advs.202003041
28. Tan J, Deng Z, Liu G, Hu J, Liu S. Anti-inflammatory polymersomes of redox-responsive polyprodrug amphiphiles with inflammation-triggered indomethacin release characteristics. *Biomaterials*. 2018;178:608–619. doi:10.1016/j.biomaterials.2018.03.035
29. Zhong P, Meng H, Qiu J, et al. αvβ3 Integrin-targeted reduction-sensitive micellar mertansine prodrug: superb drug loading, enhanced stability, and effective inhibition of melanoma growth in vivo. *J Control Release*. 2017;259:176–186. doi:10.1016/j.jconrel.2016.12.011
30. Liu Q, Liu L, Mo C, et al. Polyethylene glycol-coated ultrasmall superparamagnetic iron oxide nanoparticles-coupled sialyl Lewis X nanotheranostic platform for nasopharyngeal carcinoma imaging and photothermal therapy. *J Nanobiotechnol*. 2021;19(1):171. doi:10.1186/s12951-021-00918-0
31. Liu L, Liu L, Li Y, et al. Ultrasmall superparamagnetic nanoparticles targeting E-selectin: synthesis and effects in mice in vitro and in vivo. *Int J Nanomed*. 2019;14:4517–4528. doi:10.2147/IJN.S199571
32. Sonu G, Hamed A, Kannan MK. Detection of cancer-specific proteases using magnetic relaxation of peptide-conjugated nanoparticles in biological environment. *Nano Lett*. 2016;16:3668–3674. doi:10.1021/acs.nanolett.6b00867
33. Bai C, Jia Z, Song L, et al. Time-dependent T_1-T_2 switchable magnetic resonance imaging realized by c (RGDyK) modified ultrasmall Fe_3O_4 nanoprobes. *Adv Funct Mater*. 2018:1802281. doi:10.1002/adfm.201802281
34. Li J, Zheng L, Li C, et al. Mannose modified zwitterionic polyester-conjugated second near-infrared organic fluorophore for targeted photothermal therapy. *Biomater Sci*. 2021;9:4648–4661. doi:10.1039/D1BM00396H
35. Regimbeau M, Abrey J, Vautrot V, Causse S, Gobbo J, Garrido C. Heat shock proteins and exosomes in cancer theranostics. *Semin Cancer Biol*. 2022;86:46–57. doi:10.1016/j.semcancer.2021.07.014
36. Shao W, Yang C, Li F, et al. Molecular design of conjugated small molecule nanoparticles for synergistically enhanced PTT/PDT. *Nanomicro Lett*. 2020;12:147. doi:10.1007/s40820-020-00474-6
37. Multhoff G, Botzler C, Wiesnet M, et al. A stress-inducible 72-kDa heat-shock protein (HSP72) is expressed on the surface of human tumor cells, but not on normal cells. *Int J Cancer*. 1995;61:272–279. doi:10.1002/ijc.2910610222
38. Gross C, Koelch W, DeMaio A, Arispe N, Multhoff G. Cell surface-bound heat shock protein 70 (Hsp70) mediates perforin-independent apoptosis by specific binding and uptake of granzyme B. *J Biol Chem*. 2003;278(42):41173–41181. doi:10.1074/jbc.M302644200
39. Vega VL, Rodriguez-Silva M, Frey T, et al. Hsp70 translocates into the plasma membrane after stress and is released into the extracellular environment in a membrane-associated form that activates macrophages. *J Immunol*. 2008;180:4299–4307. doi:10.4049/jimmunol.180.6.4299
40. Chen Q-W, Liu XH, Fan J, et al. Self-mineralized photothermal bacteria hybridizing with mitochondria-targeted metal–organic frameworks for augmenting photothermal tumor therapy. *Adv Funct Mater*. 2020;30:1909806. doi:10.1002/adfm.201909806
41. Huang J, Xiao Z, An Y, et al. Nanodrug with dual-sensitivity to tumor microenvironment for immuno-sonodynamic anti-cancer therapy. *Biomaterials*. 2021;269:120636. doi:10.1016/j.biomaterials.2020.120636
42. Kawase K, Kawashima S, Nagasaki J, et al. High expression of MHC class I overcomes cancer immunotherapy resistance due to IFNγ signaling pathway defects. *Cancer Immunol Res*. 2023;11:OF1–OF14. doi:10.1158/2326-6066.CIR-22-0815
43. Mao L, Zhou -J-J, Xiao Y, et al. Immunogenic hypofractionated radiotherapy sensitising head and neck squamous cell carcinoma to anti-PD-L1 therapy in MDSC-dependent manner. *Br J Cancer*. 2023;2023:128.
44. Wang Y, Sun X, Han Y, et al. Au@MnSe(2) core-shell nanoagent enabling immediate generation of hydroxyl radicals and simultaneous glutathione deletion free of pre-reaction for chemodynamic-photothermo-photocatalytic therapy with significant immune response. *Adv Healthc Mater*. 2022;11:e2200041. doi:10.1002/adhm.202200041
45. Li Z, Cai H, Li Z, et al. A tumor cell membrane-coated self-amplified nanosystem as a nanovaccine to boost the therapeutic effect of anti-PD-L1 antibody. *Bioact Mater*. 2023;21:299–312. doi:10.1016/j.bioactmat.2022.08.028
46. Wang S, Zhang Y. HMGB1 in inflammation and cancer. *J Hematol Oncol*. 2020;13:116. doi:10.1186/s13045-020-00950-x

47. Wu L, Jin Y, Zhao X, et al. Tumor aerobic glycolysis confers immune evasion through modulating sensitivity to T cell-mediated bystander killing via TNF-alpha. *Cell Metab*. 2023;35:1580–96 e9. doi:10.1016/j.cmet.2023.07.001
48. Sun L, Kees T, Almeida AS, et al. Activating a collaborative innate-adaptive immune response to control metastasis. *Cancer Cell*. 2021;39:1361–74 e9. doi:10.1016/j.ccell.2021.08.005